J. Fluid Mech. (1990), *vol.* 215, *pp.* 601–638
Printed in Great Britain

The evolution of grid-generated turbulence under conditions of stable thermal stratification

By KYUNGHWAN YOON AND Z. WARHAFT
Sibley School of Mechanical and Aerospace Engineering, Cornell University, Ithaca, NY 14853, USA

(Received 22 March 1989 and in revised form 2 November 1989)

We investigate the evolution of grid turbulence under the action of a stable (negatively buoyant), linear, temperature profile. The experiment was carried out in a large, open circuit, low-speed wind tunnel 0.91×0.91 m^2 and 9.14 m in length specially designed for the study of stratified turbulence. The temperature gradient, formed at the entrance to the plenum chamber of the tunnel by means of an array of 72 horizontal, differentially heated elements was varied from 0 to 55 °C/m, giving a maximum Brunt–Väisälä frequency N of 1.3 s^{-1}. The grid mesh M was 2.54 cm and the mean velocity U was varied from 2.8 to 4.2 m/s. Thus the mesh Froude number $Fr_M = U/(NM)$ was varied from ∞ to 84.8 for the passive and most stable case respectively. We show that there are distinct stages in the evolution of the flow and these are determined by the turbulence Richardson number Ri_u, which is the square of the ratio of the turbulence to stratification timescales $(N\tau)^2$. For $Ri_u < 0.1$ the flow is dynamically passive and the vertical heat flux correlation coefficient $\rho_{w\theta}$ is constant with a value of -0.7. From $Ri_u \approx 0.1$ (where the turbulent potential energy is approximately 5% of the vertical kinetic energy) to $Ri_u \approx 1$ the heat flux begins to decay under the action of the buoyancy forces and the vertical velocity variance $\overline{w^2}$ decays more rapidly than for the neutral case. By $Ri_u \approx 1$ the turbulent potential energy is nearly as large as the vertical kinetic energy and the magnitude of the ratio of the buoyancy to mechanical dissipation terms in the kinetic energy budget reaches a maximum and then rapidly diminishes as the heat flux completely collapses (by $Ri_u \approx 2$). For $Ri_u > 2$ the heat flux remains small except for the most stable case studied where a significant net counter gradient heat flux occurs. Here the vertical velocity variance increases as it draws its energy from the potential energy field. For all experiments the mechanical to thermal timescale ratio remains relatively constant up until $Ri_u \approx 1$ and then increases from 1.1 to a maximum value of 2. The ratio of the r.m.s. longitudinal to vertical velocity fluctuations $(\overline{u^2})^{\frac{1}{2}}/(\overline{w^2})^{\frac{1}{2}}$, increases from the passive value (of 1.1) to a maximum of approximately 1.6 at $Ri_u \approx 1$ and then decreases as the heat flux collapses. No direct evidence of internal waves is found from the single-point measurements. The results are presented in terms of relevant lengthscale ratios determined from auto-correlation functions, spectra and from integrated quantities such as variance and dissipation rates. Particular attention is paid to a comparison with previous work, especially that of Lienhard & Van Atta (1990), the only other wind-tunnel experiment on strongly stratified grid-generated turbulence without shear. It is shown that the evolution of the flow is very sensitive to initial conditions and in order to collapse the data of different experiments the turbulence time (τ) rather than the elapsed clock time (t) must be used, i.e. the data collapse well with Ri_u but not with Nt (which is more traditionally used).

1. Introduction

The effect of stable stratification (density decreasing with height at faster than the adiabatic lapse rate) is of profound importance in geophysical and environmental flows. In the atmosphere the density decrease (resulting from a 'temperature inversion', i.e. an increase in temperature with height) frequently suppresses the turbulence and can reduce the effective diffusivity by as much as 10^6 (the ratio of the turbulent diffusivity to molecular diffusivity). Clearly, accurate prediction and control of pollution concentrations depends largely on an understanding of the underlying turbulence dynamics for these conditions. Yet proper understanding of the problem even for the simplest case, namely an initially isotropic turbulent field evolving in a region in which the (potential) temperature is increasing linearly with height is still wanting. The difficulty is most simply understood by recognizing that there is a complex interaction of two dynamic scales, one due to the mechanical turbulence, the other resulting from the stratification. We still do not have a turbulence theory that can deal adequately with more than one dominant turbulence scale be it for stratified turbulence or any other turbulent flow that is simultaneously excited or forced at more than one wavenumber.

From an experimental viewpoint the decay of initially isotropic turbulence in stratified flow also presents severe problems. For stratification effects to become important the Richardson number (defined in §2 below) must be high, i.e. lengthscales and density differences must be large compared with velocity differences (or fluctuations). In the atmosphere the large vertical lengthscale generally ensures that buoyancy effects play a major role, but in the laboratory, with its proscribed lengthscale, strong stable stratification can only be achieved using large density gradients and relatively small velocities. For this reason most stratified experiments have been done using salt-stratified water. Much of this work is reviewed by Itswiere, Helland & Van Atta (1986) and Hopfinger (1987). Recently, however, Lienhard & Van Atta (1990) (see also Lienhard 1988) have shown that large temperature gradients may be achieved in air tunnels and that this flow has many advantages over stratified salt-water experiments. Their work and its relation to the present experiment will be discussed after we briefly review the salt-water stratified experiments.

Salt-stratified water experiments fall into two categories; transient, where the grid is pulled or dropped through the stationary fluid, and steady state, where the fluid is moving in a channel and the turbulence characteristics are not changing with time. The former experiments, notably by Dickey & Mellor (1980), who dropped a biplane grid through a stratified fluid and Britter *et al.* (1983), who dragged a grid through the fluid, while yielding interesting data, particularly on the velocity decay rate, provided relatively little information on turbulent transport and spectral characteristics. Steady state salt-stratified experiments have been carried out by Stillinger *et al.* (1983*b*) and by Itswiere *et al.* (1986) in a ten-layer, salt-stratified water closed loop channel described by Stillinger *et al.* (1983*a*). These experiments revealed new information on spectra, mass transfer and the evolution of the velocity field. They showed that as the flow evolves the turbulence becomes fossilized and internal waves appear. Their results are presented in terms of predictions of Gibson (1980) and good agreement is found. Of particular relevance to the present work is that regions of counter gradient mass flux were observed. However, these experiments, too, have problems. As discussed in Itswiere *et al.* (1986), waves initially generated at the grid affected the velocity fluctuation decay rates observed by

Stillinger *et al.* (1983*b*). Furthermore, Lienhard (1988) notes that scalar dissipation is difficult to measure because of the small diffusivity of the salt, the experiments are not truly steady since the density profile degrades with time, and sample times are further limited because of bubble formation on the hot film sensors. Thus spectral and variance data is lacking in accuracy because of the limited sampling duration.

Such considerations motivated the wind-tunnel work of Lienhard & Van Atta (1990) as well as the present work. The two experiments have much in common although they were conceived and carried out independently. It was while completing our experiments that we received Lienhard (1988) and Lienhard & Van Atta (1990, hereinafter referred to as LV) and their work has had considerable influence on the reporting of our own results. As far as we know LV and our experiment are the only ones that investigate strongly stratified wind-tunnel turbulence, an earlier experiment by Montgomery (1974) achieving only moderate stratification effects. (Webster (1964) examined stratified wind-tunnel turbulence but his experiment also contained shear, not the subject of the present work.)

The results of LV and the present experiment show qualitative similarity in the evolution of the variances and fluxes and other single-point quantities, but there are also some significant differences and one of our objectives here will be to compare the two experiments critically. The apparatus for the experiments is quite different: LV generated their gradient using a fin-tube cross-flow heat exchanger with a shear controller (Lienhard 1988) while we used a system of heated rods, similar to the toaster used by Sirivat & Warhaft (1983). The details of our apparatus are given in §3. Given these differences in the mode of generation of the temperature gradient, as well as the differences in tunnel characteristics, a comparison of the two experiments provides insight into the sensitivity of the flow evolution to initial conditions, a vitally important aspect in fluid mechanics.

Apart from experiments, there have been a number of numerical attempts to examine the decay of stratified turbulence. Riley, Metcalfe & Weissmann (1981) provide extensive results obtained from direct numerical solutions of the Navier–Stokes equations. Métais (1987) has done a comparison of direct simulations, large-eddy simulations and a two-point closure model (E.D.Q.N.M.) but their results are less complete than Riley *et al.* (1981), and Sanderson, Hill & Herring (1987) have used the direct interaction approximation to examine the problem. Recently Rogers (private communication 1989) has carried out high resolution direct simulations. We will compare our results with these simulations where appropriate.

The broad objective of the present paper is, then, to study experimentally the effect of a stable density gradient in isotropic grid-generated turbulence. We pay particular attention to initial conditions by both varying them in our own work and comparing our experiment to LV, the only other strongly stratified wind-tunnel experiment. Finally, we note, that the work in many respects is an extension of our earlier experiment on the evolution of heat flux and temperature variance under the action of a passive linear temperature profile (Sirivat & Warhaft 1983).

2. Governing equations and scale relations

In reporting our results emphasis will be placed on the evolution of single-point quantities such as variances, co-variances and their related lengthscales and timescales. Although a number of these lengthscales were originally determined from dimensional considerations and simple physical models (Kolmogorov 1961; Ellison 1957; Dougherty 1961; Ozmidov 1965; Gibson 1987), their significance can best be

seen from the governing second-order turbulence equations (Lumley & Panofsky 1964; Monin & Yaglom 1971; Hopfinger 1987; Lienhard & Van Atta 1990). Here we outline the conceptual framework developed by the above workers in a form suitable for the presentation of our data.

We consider the evolution of grid-generated turbulence under the influence of a linear stable density profile. This is the simplest situation in which to study the effects of stratification on turbulence; there is no shear and the turbulence is initially (before the buoyancy effects begin to play a role) close to isotropic. Assuming homogeneity in the vertical (y, z)-plane (a sketch of the tunnel with the coordinate system is given in §2), the equations for the averaged turbulence kinetic energy $k = \frac{1}{2}(\overline{u^2}+\overline{v^2}+\overline{w^2})$ and its components $\frac{1}{2}\overline{u^2}$, $\frac{1}{2}\overline{v^2}$ and $\frac{1}{2}\overline{w^2}$, the kinematic vertical heat flux $\overline{\theta w}$ and the mean squared temperature variance, $\overline{\theta^2}$, are (e.g. Lumley & Panofsky 1964),

$$U\frac{\partial k}{\partial x} = \frac{g}{T_0}\overline{\theta w} - \epsilon, \tag{1a}$$

$$U\frac{\partial(\frac{1}{2}\overline{u^2})}{\partial x} = -\frac{1}{\rho_0}\overline{p\frac{\partial u}{\partial x}} - \nu\overline{\frac{\partial u}{\partial x_j}\frac{\partial u}{\partial x_j}}, \tag{1b}$$

$$U\frac{\partial(\frac{1}{2}\overline{v^2})}{\partial x} = -\frac{1}{\rho_0}\overline{p\frac{\partial v}{\partial x}} - \nu\overline{\frac{\partial v}{\partial x_j}\frac{\partial v}{\partial x_j}}, \tag{1c}$$

$$U\frac{\partial(\frac{1}{2}\overline{w^2})}{\partial x} = -\frac{1}{\rho_0}\overline{p\frac{\partial w}{\partial x}} - \nu\overline{\frac{\partial w}{\partial x_j}\frac{\partial w}{\partial x_j}} + \frac{g}{T_0}\overline{\theta w}, \tag{1d}$$

$$U\frac{\partial\overline{\theta w}}{\partial x} = -\overline{w^2}\beta + \frac{g}{T_0}\overline{\theta^2} - \frac{1}{\rho_0}\overline{\theta\frac{\partial p}{\partial z}}, \tag{2}$$

$$U\frac{\partial(\frac{1}{2}\overline{\theta^2})}{\partial x} = -\overline{\theta w}\beta - \epsilon_\theta. \tag{3}$$

Here U is the mean velocity (in the x-direction) which is constant throughout (except in the boundary layers of the tunnel which are very small compared to the free-stream region and are not of interest in this study); g is the acceleration due to gravity (acting in the $-z$-direction), T_0 and ρ_0 are the reference temperature and density respectively; u, v and w are the longitudinal, transverse and vertical fluctuating velocity components, θ is the fluctuating temperature, $\beta \equiv \mathrm{d}T/\mathrm{d}z$ is the vertical temperature gradient, p is the fluctuating pressure, ϵ is the dissipation rate of the velocity fluctuations ($\equiv \nu\overline{(\partial u_i/\partial x_j)(\partial u_i/\partial x_j)}$ where ν is the kinematic viscosity) and ϵ_θ is the destruction rate of temperature variance by molecular smearing ($\equiv \alpha\overline{(\partial\theta/\partial x_j)(\partial\theta/\partial x_j)}$ where α is the thermal diffusivity). The overbars represent averaging. Note that, from continuity, the pressure terms in the component kinetic energy equations sum to zero in the total kinetic budget (equation (1*a*)). The molecular diffusion and triple moment transport terms have been neglected in equations (1*a*), (2) and (3), since, using simple scaling arguments (Tennekes & Lumley 1972), they can always be shown to be small compared with the other terms in evolving grid turbulence (Budwig, Tavoularis & Corrsin (1985) estimated for their passive temperature experiments in grid turbulence, that these terms are respectively 10^{-7} and 10^{-5} the production term). The neglect of the destruction term $(\nu+\alpha)\overline{(\partial\theta/\partial x_j)(\partial w/\partial x_j)}$ in (2) is less certain. It is negligible in high-Reynolds-number

flows on the assumption that θ and w are poorly correlated at the small scales (local isotropy) but in this moderate-Reynolds-number flow, with stratification further reducing the gap between the large and small scales, this term may not be negligible. Unfortunately, it is difficult to determine experimentally. It should be noted that (as a consequence of equation (2)) if the turbulence is homogeneous in the z-direction and β is initially constant then β will remain constant and is independent of x. This was first pointed out by Corrsin (1952).

The physical significance of the terms in the above equations is described in the standard texts (Lumley & Panofsky 1964; Monin & Yaglom 1971). The gravitational terms (first term on the right-hand side of (1a) and second term on the right-hand side of (2)) have a profound effect on the development of the velocity and thermal fields. For the passive case these terms are negligible by definition. This situation has been studied in detail by Sirivat & Warhaft (1983) (and by others referred to therein). In particular Sirivat & Warhaft studied the influence of varying the thermal scale relative to the velocity scale on the evolution of the flow. The sensitivity to initial conditions will be a particular focus of the present study.

Equation (1a) shows that the change of turbulent kinetic energy is caused by dissipation at the small scales and by the buoyancy term. This latter term is initially negative (for passive flows the correlation coefficient between θ and w, $\rho_{\theta w}$ is around -0.7 (Sirivat & Warhaft 1983; Budwig *et al.* 1985). Thus we would expect that when buoyancy plays a role the kinetic energy should decay more rapidly than for the neutral case. However, the (negative) buoyancy causes the heat flux to collapse (equation (2)) and may cause it to change sign, thereby turning the buoyancy destruction term in equation (1a) into a source term. We will show this can result in an increase in $\overline{w^2}$ as the flow evolves.

Equation (3) can be rewritten as a rate equation for fluctuating potential energy (PE) per unit mass (e.g. Riley *et al.* 1981)

$$U\frac{\partial(\mathrm{PE})}{\partial x} = \frac{-g}{T_0}\overline{\theta w} - \frac{g}{T_0}\beta^{-1}\epsilon_\theta. \tag{4}$$

Notice that when the heat flux term is a sink in the vertical kinetic energy budget, it is a source in the potential energy budget and vice versa. The sum of (1a) and (4) give the total rate of change of energy per unit mass (E)

$$U\frac{\partial E}{\partial x} = -\frac{g}{T_0}\beta^{-1}\epsilon_\theta - \epsilon, \tag{5}$$

where $E = k + (g/T_0)(\frac{1}{2}\overline{\theta^2})\beta^{-1}$. Of particular interest is the total vertical fluctuating energy per unit volume, e_z which is

$$e_z = \tfrac{1}{2}\rho_0\left(\overline{w^2} + \frac{g}{T_0}\overline{\theta^2}\beta^{-1}\right). \tag{6}$$

While for the passive case there is only a single integral velocity lengthscale (the separate thermal integral lengthscale does not affect that of the velocity field, Sirivat & Warhaft 1983), the situation is much more complex for the active situation. For the stratified case the imposed parameters for the flow are the mean velocity U, the grid mesh length M and the stratification parameter. (Another parameter forming the turbulence is the grid solidity, σ. While M determines the integral scale of the turbulence σ determines whether the region close to the grid will be more 'wake like' or 'jet like'. Nearly all workers (Comte-Bellot & Corrsin 1966; Hinze 1975) use a

value between 0.3 and 0.4 (coalescing wakes). See §2 below.) The stratification parameter is usually expressed in the form of the Brunt–Väisälä frequency $N \equiv [(-g/\rho_0)\,\partial\bar{\rho}/\partial z]^{\frac{1}{2}} = [(g/T_0)\,\beta]^{\frac{1}{2}}\,\mathrm{s}^{-1}$. For the passive case $N \approx 0$. While the mesh size M determines the initial scale of the velocity fluctuations, their subsequent evolution is determined by the complex interaction of the turbulence dissipation and the stable stratification, the latter, we will show, assuming an ever increasing role as the flow evolves (close to the grid the flow behaves passively).

In order to determine the relevant lengthscales for the stably stratified flow we write (6) as

$$e_z = \tfrac{1}{2}\rho_0\,\overline{w^2}(1 + (g/T_0)\,(\overline{\theta^2}/\overline{w^2})\,\beta^{-1}) = \tfrac{1}{2}\rho_0\,\overline{w^2}(1 + (L_\theta/L_\mathrm{b})^2), \tag{7}$$

where $L_\mathrm{b} \equiv (\overline{w^2})^{\frac{1}{2}}/N$ and $L_\theta \equiv (\overline{\theta^2})^{\frac{1}{2}}/\beta$. Clearly, for $L_\theta \ll L_\mathrm{b}$ the flow is passive and all the fluctuating energy is kinetic. As L_θ/L_b increases the buoyancy effects will become significant. One of the main objectives of this work is to determine how the flow dynamics vary as L_θ/L_b is increased. L_b is known as the buoyancy lengthscale (see, for example, Hopfinger 1987; Lienhard & Van Atta 1990) and is a measure of the upper limit the particles having ambient kinetic energy can move in the vertical, against the temperature gradient. L_θ is known as the over-turning scale and is a measure of the local potential energy of the flow (Ellison 1957). Note that while for a passive temperature gradient, $L_\mathrm{b} \to \infty$ and therefore is irrelevant, L_θ is still the defining thermal lengthscale (Sirivat & Warhaft 1983). However, for the active case the evolution of L_θ will vary quite differently from that of the passive case since, for a fixed temperature gradient (β), the stratification destroys the heat flux (equation (2)) and hence the production term for $\overline{\theta^2}$ (equation (3)) will also be diminished.

In grid-generated turbulence to be studied here, the turbulence energy containing scale L (to be defined below) is set by the grid mesh and is initially independent of L_b and L_θ. As the flow evolves L grows and L_b diminishes. The ratio $L_\mathrm{b}/L = (\overline{w^2})^{\frac{1}{2}}/(NL)$ defines the turbulence Froude number, Fr_t. For $Fr_\mathrm{t} \approx 1$ the vertical motion will be strongly affected by the buoyancy. Alternatively the ratio $(L/L_\mathrm{b})^2 = (g/T_0)\,\beta/(\overline{w^2}/L^2)$ can be used to define a turbulence Richardson number, Ri_w, for the shearless flow. Another related Richardson number $Ri_u = (g/T_0)\,\beta/(\overline{u^2}/L^2)$ will be used extensively in our analysis. We note that $\overline{w^2}/\overline{u^2}$ is always of order one so $Ri_u \approx R_w$. Note that Ri_u can be considered to be the ratio of the square of the timescale of the turbulence ($\tau = L/(\overline{u^2})^{\frac{1}{2}}$) to that of the stratification ($1/N$).

While there is general agreement concerning the definition of L_θ and L_b there are a number of ways of defining the integral scale L. For passive turbulence these various definitions are simply related but for the active case their relationship to each other is less obvious.

(*a*) L can be obtained from the (time) velocity auto-correlation function by integrating up to its first zero (for u) and second zero crossing (for w) (Comte-Bellot & Corrsin 1971; Sirivat & Warhaft 1983). Taylor's frozen hypothesis is used to convert from a timescale to a lengthscale. The resultant integral scales are L_f and L_g (sometimes called L_{11} and L_{12}) for u and w respectively.

(*b*) L can also be obtained from the velocity fluctuations and the energy dissipation rate ϵ. There are two often used definitions; $L_k \equiv k^{\frac{3}{2}}/\epsilon$ and $L_u \equiv (\overline{u^2})^{\frac{3}{2}}/\epsilon$. In isotropic turbulence ($\overline{u^2} \approx \overline{v^2} \approx \overline{w^2}$) thus $L_k = 1.84\,L_u$. For the stratified case the turbulence is anisotropic and the ratio L_k/L_u varies with N and x. In the above definitions of L_u and L_k the energy dissipation rate is determined from the velocity spectrum (see §§3 and 4 below). We note that L_u and L_k are traditionally associated with the notion of an inertial cascade in high-Reynolds-number turbulence. Here the

flow is of moderate Reynolds number and moreover the buoyancy forces further reduce the large- and small-scale separation. However, their definition is unambiguous and their value can be measured precisely for this flow too. It is indeed one of our objectives to examine how these scales depart from their values in neutral grid turbulence.

In the work to follow we will study the relationship between the various definitions of the integral scale. Their ratios are affected by the stratification but they are always of order unity. Unless we specify, when we refer to L we will have in mind L_u since this one is the most commonly used in the literature.

There is yet one more scale effective at the low wavenumbers, the Dougherty–Ozmidov Scale (Dougherty 1961; Ozmidov 1965)†; $L_{\mathrm{DO}} \equiv (\epsilon/N^3)^{\frac{1}{2}}$. At this scale the buoyancy and inertial forces of the turbulence are approximately equal. For $L_{\mathrm{DO}} > L$ the turbulence is not affected by the stratification. This is similar to the relation between L_{b} and L. Note that $(L_{\mathrm{DO}}/L_{\mathrm{b}}) = (\epsilon/N\overline{w^2})^{\frac{1}{2}}$. If we write $\epsilon = (\overline{u^2})^{\frac{3}{2}}/L_u$ and assume $\overline{w^2} \approx \overline{u^2}$ (our results will show they are of the same order even for the strongest stratification) then it follows that $L_{\mathrm{DO}}/L_{\mathrm{b}} \approx (Fr_{\mathrm{t}})^{\frac{1}{2}}$ or $L_{\mathrm{DO}}^2 \approx L_{\mathrm{b}}^3/L_u$. Thus for $L_u > L_{\mathrm{b}}$, $L_{\mathrm{DO}} < L_{\mathrm{b}}$ and for $L_u < L_{\mathrm{b}}$, $L_{\mathrm{DO}} > L_{\mathrm{b}}$.

At the high wavenumber region of the spectrum there is the Kolmogorov dissipation scale $\eta \equiv (\nu^3/\epsilon)^{\frac{1}{4}}$. Fortunately, this is close to the thermal dissipation scale, or Corrsin scale $\eta_\theta \equiv (\kappa^3/\epsilon)^{\frac{1}{4}}$ since $\kappa \approx \nu$ for air. Thus there is only one microscale to consider.

The plethora of scales is daunting and part of the objective of this work is to describe the flow in terms of the least number of ratios of these scales. It should be apparent that it is the relation of the integral scale L to the buoyancy scale L_{b} and over turning scales L_θ that is of special significance. Thus, particular attention will be given to the ratios L_{b}/L_θ, L_{b}/L and L_θ/L.

3. Experimental apparatus and instrumentation

3.1. *The wind tunnel and heater*

The experiment was carried out in a new large, low-speed, low-background-turbulence wind tunnel specially designed for stratified flow studies. A sketch of the tunnel is shown in figure 1. Apart from the heater element section the tunnel is of standard open circuit suction design. The test section was 91×91 cm^2 and 9.1 m long. The large cross-section area allowed for a large homogeneous core to persist to the end of the tunnel in spite of the development of the boundary layers. The mesh length M of the square bar biplanar brass grid was 2.54 cm, giving a longitudinal tunnel extent of $360M$ and vertical and horizontal dimensions of $36M$. The solidity of the grid (ratio of closed to projected area) was 0.34. One of the sidewalls of the tunnel was slightly divergent (pitch angle 0.3° maximum) to ensure a constant centreline mean speed with the development of the boundary layer. The test section was wooden (1.9 cm plywood) and covered with 5.08 cm thick fibre-glass insulating sheets. Measurements were carried out by inserting the probes through 17 holes (placed $20M$ apart) on the sidewalls and 9 holes on the top and bottom walls (the latter for homogeneity measurements). The test section exited to a diffuser section in which a smooth transition was made from the square to a circular section to house

† This has been traditionally known as the Ozmidov scale. However, it was defined earlier by Dougherty. The two derivations are somewhat different; Dougherty considers the turbulence spectrum and works in wavenumber space while Ozmidov works in physical space. We thank John Lumley for bringing the Dougherty paper to our attention.

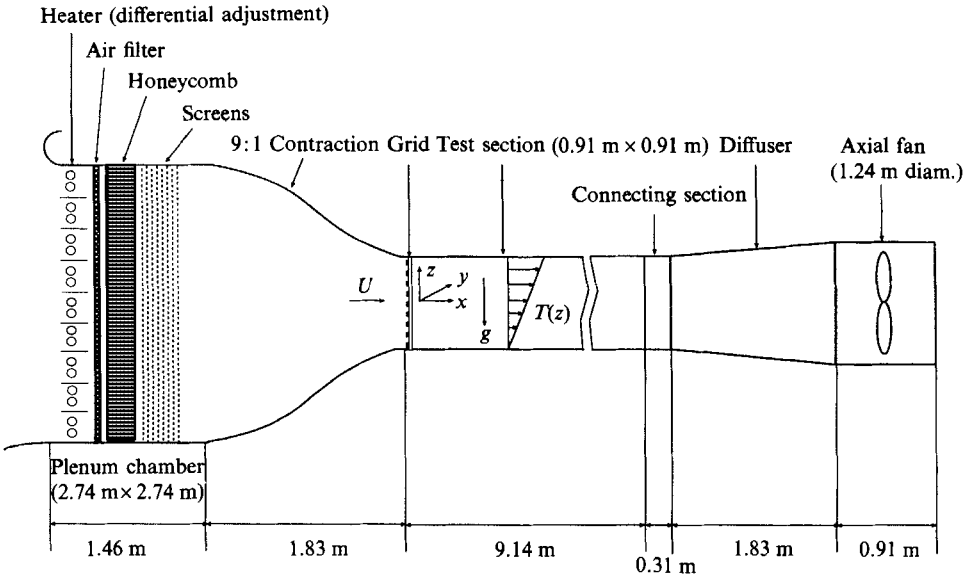

FIGURE 1. Sketch of the stratified wind tunnel. Note, there are 72 heater elements (only 18 are shown in the sketch).

a 48 in. diameter axial fan (Buffalo Forge Co.). Between the end of the test section and the diffuser a fine screen was placed to avoid separation at the entrance to the diffuser. For our experiment the mean test section velocity was varied from 3 to 6 m/s but the tunnel can achieve a velocity of up to 20 m/s. The hot air was exited to a large laboratory bay. In some experiments it was exhausted through a window to the outside to avoid unwanted feedback.

The design principle of the heater, plenum and contraction was to produce a linear temperature profile in as low background turbulent flow as possible so that by the time the flow reached the grid there would be a linear temperature profile in (almost) laminar flow. Thus the temperature fluctuations in the test section would be due solely to the action of the grid-generated turbulence against the temperature gradient. This is the same as the 'toaster' approach used by Sirivat & Warhaft (1983) although here, because of the larger gradient required, a different heater design was neccssary.

The heater, placed at the entrance to the plenum, consisted of 72 horizontal 2.74 m long, equally spaced elements. They were nichrome ribbons inserted through 9.53 mm outsider diameter porcelain tubes. The ribbons were 0.127 mm thick and 6.35 mm wide for the top 32 elements (where more heat was required) and 0.1 mm × 4.76 mm for the bottom 40 elements. Their resistances were 1.37 and 2.26 Ω/m respectively (at room temperature). Black aluminium plates of cross-section area 20.3 cm × 1.6 mm were placed horizontally between every second element to reduce radiation losses (see figure 1. Note that only 18 of the 70 elements are shown in the sketch). The heater elements were differentially controlled to produce the linear temperature profile. A trial and error 'tuning' approach was used to obtain the linear profile. The top 32 rods could be heated to 5 kW maximum and the bottom 40 rods to 2.5 kW. The total power required for the largest temperature gradient used (55 °C/m) was approximately 60 kW. Three thin vertical aluminium

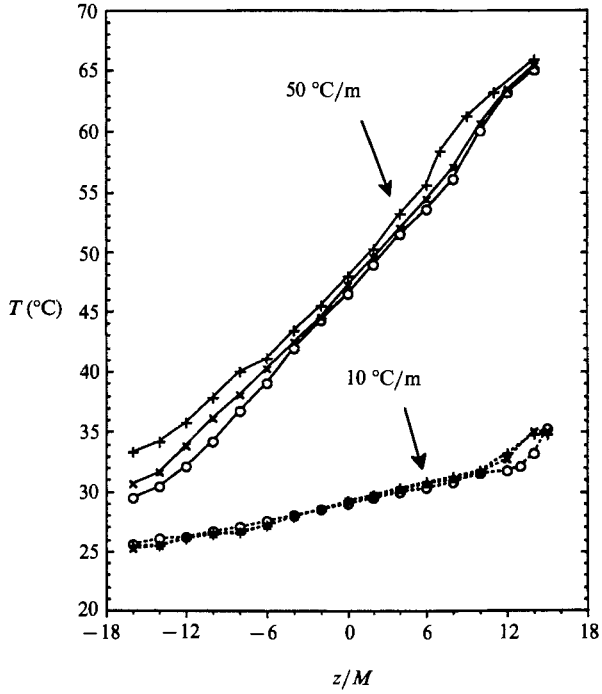

FIGURE 2. Mean temperature profiles at various downstream positions for $\beta = 50$ °C/m and 10 °C/m, $U = 3.5$ m/s. ○, $x/M = 36.5$; ×, $x/M = 156.5$; +, $x/M = 276.5$.

rods were equally spaced and fastened to the heating rods in order to stop sagging of the elements. Further design details are in Yoon (1989).

The heated air produced by the elements first passed through an air filter which removed all particles down to 1 μm. To reduce swirl and lateral mean velocity fluctuations the air then passed through a low heat conductivity (polycarbonate) set of honeycombs of 1.905 cm cell diameter and 15.24 cm length. This was followed by eight fine wire screens in order to dampen the turbulence. The solidity of the screens was 0.373, their wire diameter was 0.165 mm and their mesh size was 0.0794 cm. They were placed 7.6 cm apart (i.e. approximately 100 screen mesh lengths) so that ample decay occurred before the next screen (Weighart 1953). After the screens the flow was accelerated through the 9:1 axisymmetric contraction. Both the plenum chamber and the contraction section were insulated with fibre-glass sheets to avoid heat loss.

3.2. *The transducers and data acquisition system*

Mean velocity and temperature were measured using standard Pitot tubes and Chromel–Constantan thermocouples. The longitudinal and vertical velocity fluctuations, u and w, were measured with a 90° cross-hot-wire array in conjunction with Dantec 55 M01 constant temperature bridges. The length to diameter ratio of each of the 3.05 μm diameter tungsten wires was 200 and their spacing was approximately 1 mm. The fluctuating temperature was measured with a platinum wire with a diameter of 1.27 μm and length to diameter ratio of 400. It was placed 0.5 mm from the cross-array and connected to an a.c. fast response temperature bridge. All wires

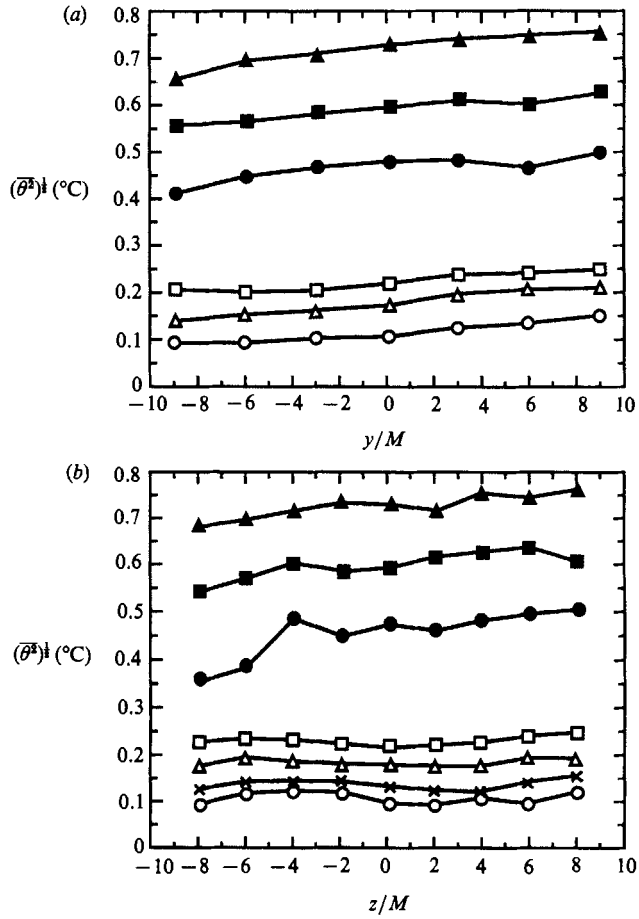

FIGURE 3. Profiles of the r.m.s. of the temperature fluctuations. (*a*) Transverse homogeneity; (*b*) vertical homogeneity. Solid symbols are for the case 50 °C/m, 3.5 m/s; open symbols are for 10 °C/m, 3.5 m/s. ●, $x/M = 36.5$; ■, $x/M = 156.5$; ▲, $x/M = 276.5$; ○, $x/M = 36.5$; ×, $x/M = 76.5$; □, $x/M = 156.5$; △, $x/M = 276.5$.

lay in the vertical plane, the temperature wire normal to the mean flow and the cross-wires 45° to the normal (Yoon 1989).

A special calibration tunnel was built in order to calibrate the cross- and temperature-wires over the range of velocities and temperatures used in the experimental flow. The cross-wire was rotated between −10° and 10° from the normal probe position in order to determine the yaw angle coefficient. The method of approach was similar to that of Champagne & Sleicher (1967) and Champagne, Sleicher & Wehermann (1967). The cross-wire data was corrected point by point for temperature fluctuation contamination using a modified form of King's law with temperature dependent coefficients (Perry 1982; Yoon 1989). The temperature wire was operated at a sufficiently low overheat that no correction for velocity contamination was necessary for the relatively small velocity fluctuations in this flow. Full details of the calibration procedure are in Yoon (1989).

The three channels of amplified a.c. signals (cross-wire and temperature probe) were digitized (DEC, ADV-11DA) within ±10 V scale and with a resolution of 4.88 mV (12 bits) and a maximum speed of approximately 45 kHz. The data was

then analysed on a MicroVax II computer. The sampling frequency per channel was varied between 2 kHz and 5 kHz (depending on the mean speed of the flow) so that scales beyond the Kolmogorov scale could be resolved. Each block of data contained 2048 samples and 100 blocks were analysed at each measurement point. Thus variance and co-variance estimates were made from 2.048×10^6 points. The co- and quadrature-spectral estimates were determined by fast Fourier transforming each data block. One hundred of these were averaged to produce the final spectrum. The FFT procedure used was the same as that described in Bendat & Piersol (1971, chapter 9).

3.3. *Wind tunnel performance*

The turbulence intensity $(\overline{u^2})^{\frac{1}{2}}/U$ of the flow just before the grid was 0.25% and the background temperature noise (heaters off) was approximately 0.025 °C r.m.s. The centreline mean velocity (after adjusting the sidewall) varied by $\pm 0.5\%$ over the tunnel length. At the furthest downstream measurement station ($340M$) the boundary layer was $6M$, still providing a large core flow since the tunnel area is $36 \times 36M$.

Figure 2 shows the mean temperature profiles for two cases ($\beta = 10$ and 50 °C/m). The mean temperature (for a fixed z) varies by less than 5% along the tunnel and the gradient in the z-direction is remarkably stable and constant over at least $12M$ in the z-direction (for the worst case). Figure 3 shows the transverse and vertical temperature variance profiles for the above two cases. There is a small asymmetry of approximately $\pm 4\%$ in the horizontal profiles (figure 3*a*) which is possibly due to the proximity of the laboratory wall on the positive y-side of the tunnel. The vertical homogeneity varies by about $\pm 5\%$ across the core of the flow, a value comparable to that observed by Sirivat & Warhaft (1983) in their passive gradient experiments. The variation of the velocity variances across the core of the flow was approximately $\pm 4\%$ in the vertical and horizontal directions (Yoon 1989).

4. The results

As explained in §2, the emphasis of this work will be on the evolution of single-point quantities such as variances, co-variances and their related lengthscales. Spectra and correlation functions will be used to provide insight into lengthscale evolution but spectral dynamics will not be investigated in any detail. We will begin by describing the velocity field and this will be followed by the temperature variance and heat flux evolution. The various stably stratified cases will be compared with the neutral case. In §5 we will show how the data may be collapsed using the various scales described in §2 and we will compare our results to those of other workers using these normalization procedures.

Table 1 lists the flow parameters for the neutral flow and the five stratified cases investigated. A more detailed tabulation of the variances, co-variances, lengthscales, etc. for these flows is given in an Appendix.† From here on we will refer to the various flow stratifications in terms of the mean Froude number based on the grid mesh length, $Fr_M \equiv U/(NM)$. The columns in table 1 are in order of increasing stratification (decreasing Fr_M). The first column is for the passive case.

† Copies of the Appendix, which is not reproduced here, are available on request from either the authors or the Editor.

Fr_M	$U/(NM)$	∞	253	192	127	114	84.8
U	m/s	3.5	3.5	3.9	4.2	3.6	2.8
β	dT/dz (°C/m)	0	9	20	55	50	55
T_0	°C	23.8	25.3	33.5	45.1	48.5	45.1
Re_M	UM/ν	5780	5670	6040	6070	5100	4050
$N(s^{-1})$	$(g\beta/T_0)^{\frac{1}{2}}$	0	0.544	0.799	1.30	1.24	1.30
r.m.s. u	m/s($\times 10^{-2}$)	5.38	5.39	6.07	7.09	5.92	3.87
r.m.s. w	m/s($\times 10^{-2}$)	4.82	4.77	5.90	5.67	4.38	2.85
ϵ	m^2/s^3($\times 10^{-3}$)	9.31	9.53	10.64	16.06	9.75	2.85
$L_u(=(\overline{u^2})^{\frac{3}{2}}/\epsilon)$	m($\times 10^{-3}$)	16.7	16.4	21.0	22.2	21.3	20.4
λ	m($\times 10^{-3}$)	8.47	8.48	9.22	9.09	9.84	11.8
$\eta=(\nu^3/\epsilon)^{\frac{1}{4}}$	m($\times 10^{-3}$)	0.790	0.798	0.802	0.762	0.877	1.18
Re_L	$(\overline{u^2})^{\frac{3}{2}}L_u/\nu$	58.5	56.4	77.7	89.6	70.3	44.9
Re_λ	$(\overline{u^2})^{\frac{1}{2}}\lambda/\nu$	29.6	29.2	34.1	36.7	32.5	25.9
τ_k(s)	$2k/\epsilon$	0.811	0.784	1.00	0.814	0.917	1.34
r.m.s. θ	°C	—	0.115	0.222	0.684	0.597	0.562
ϵ_θ	$°C^2/s$	—	0.0194	0.0537	0.630	0.400	0.272
τ_θ(s)	θ^2/ϵ_θ	—	0.682	0.914	0.743	0.893	1.16
r	τ_k/τ_θ	—	1.15	1.09	1.10	1.03	1.16
Ri_u	$N^2L_u^2/\overline{u^2}$	0	0.0274	0.0764	0.166	0.199	0.471
$\overline{u^2}/U^2$	A	0.0712	0.0676	0.0631	—	—	—
$=A(x/M)^{-n}$	n	1.31	1.29	1.27	—	—	—
$\overline{w^2}/U^2$	A	0.0652	0.0615	0.0683	—	—	—
$=A(x/M)^{-n}$	n	1.34	1.34	1.32	—	—	—

TABLE 1. Flow parameters. $M = 0.0254$ m (turbulence parameters (r.m.s. u, ϵ, etc.) were calculated at $x/M = 76.5$). ϵ and ϵ_θ were calculated from spectra (see text for details); λ is the Taylor microscope.

A note on scaling

Traditionally in grid turbulence the flow field evolution is plotted as function of x/M (Comte-Bellot & Corrsin 1966; Sirivat & Warhaft 1983). However, when buoyancy effects are important it is more appropriate to normalize the elapsed time from the grid ($t = x/U$) with the stratification timescale $\tau_B (=2\pi/N$, the Brunt–Väisälä period). Lienhard & Van Atta (1990) show that their data collapse well using this normalization. We will show that our data also collapse well using this scheme, however they are shifted (in the negative t/τ_B direction) with respect to the data of LV. The reason for this mismatch will be described in detail in §5 where we will show that the turbulence timescale $\tau = L/(\overline{u^2})^{\frac{1}{2}}$ rather than the clock time, t, is the more appropriate parameter with which to describe the flow evolution in stratified turbulence, i.e. we will use τ/τ_B (rather than t/τ_B) as the non-dimensional time. Here we note that if the turbulence decay follows a power law ($\overline{u^2} \propto t^{-n}$ where n is constant) then $\tau \propto t$. This is the case in passive grid turbulence after approximately 30 mesh lengths from the grid where the power law decay begins. However, close to the grid, a region that appears to be very important in determining the subsequent development of the flow for the stratified cases (§5 below), the turbulence energy decay is very rapid and does not follow a power law decay. Thus the clock time and the turbulence timescales are not proportional. Furthermore, for the stratified cases, the power law decay is violated far downstream and here, too, t is not proportional to τ.

The procedure for plotting the data will be as follows. In §§4.1 and 4.2 we will use x/M and $N't$ as the abscissa (where $N' = N/2\pi$), the former for passive data ($N \to 0$)

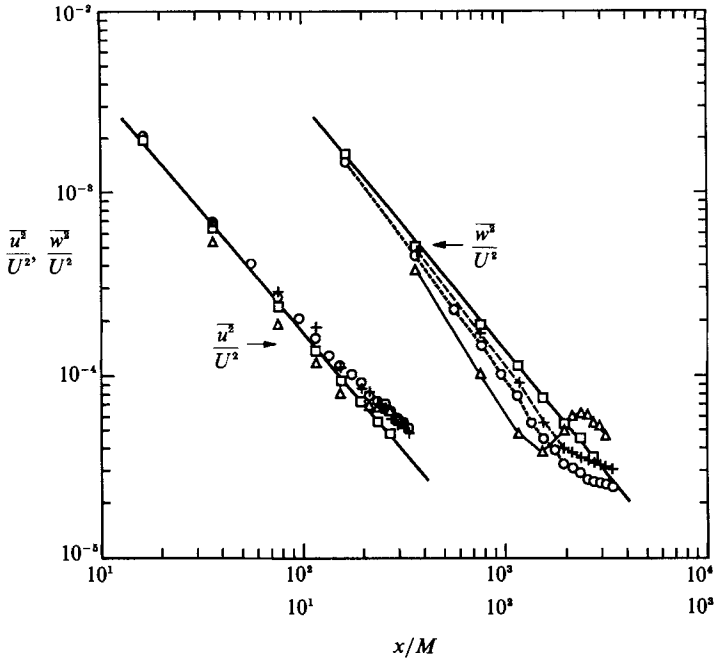

FIGURE 4. The longitudinal velocity variance, $\overline{u^2}/U^2$ and vertical velocity variance, $\overline{w^2}/U^2$ as a function of x/M. The straight line is the best fit for a number of passive cases. △, $Fr_M = 84.8$; ○, $Fr_M = 114$; +, $Fr_M = 127$; □, $Fr_M = \infty$ (passive case).

and for the velocity field. Following LV we will use $N't$ for the stratified cases in order to show that this provides a convenient framework for the data and in order to contrast the differences between our work and that of LV, the only other wind-tunnel stratified experiment. However, exceptions to this scheme will be made where we wish to emphasize a particular aspect. Finally, in §5 we will show how all the data can be made compatible using the turbulence rather than the clock timescale.

4.1. *The velocity field*

Figure 4 shows the evolution of the longitudinal and vertical velocity variances, $\overline{u^2}/\overline{U^2}$ and $\overline{w^2}/\overline{U^2}$, for the various stratified cases, plotted as a function of x/M. The straight line is the best fit for a number of passive experiments. The decay law for the passive case (table 1) compares well with our previous results (Sirivat & Warhaft 1983) and those of other workers (Comte-Bellot & Corrsin 1966). For the active cases the longitudinal variance tends to decrease at a slower rate than for the passive cases far downstream ($x/M > 200$) and for the case with the lowest Fr_M ($=84.8$), i.e. the highest stability, $\overline{u^2}/\overline{U^2}$ drops slightly below that of the passive case until approximately $x/M = 200$ and then it rises above it. As would be expected the effects of the negative buoyancy are far more pronounced for the vertical variance, although the trend is similar to that of $\overline{u^2}/\overline{U^2}$. The data show three stages: initially the variance decays at approximately the same rate as for the passive case, it then decays more rapidly as the buoyancy effects become more pronounced and finally ($x/M \approx 200$) the variance begins to decay at a much slower rate than for the passive flow. Notice for the strongest stability, far downstream $\overline{w^2}$ actually increases indicating that vertical kinetic energy is being supplied to the flow, i.e. the kinetic energy extracted earlier from the flow by the negative buoyancy is being fed back.

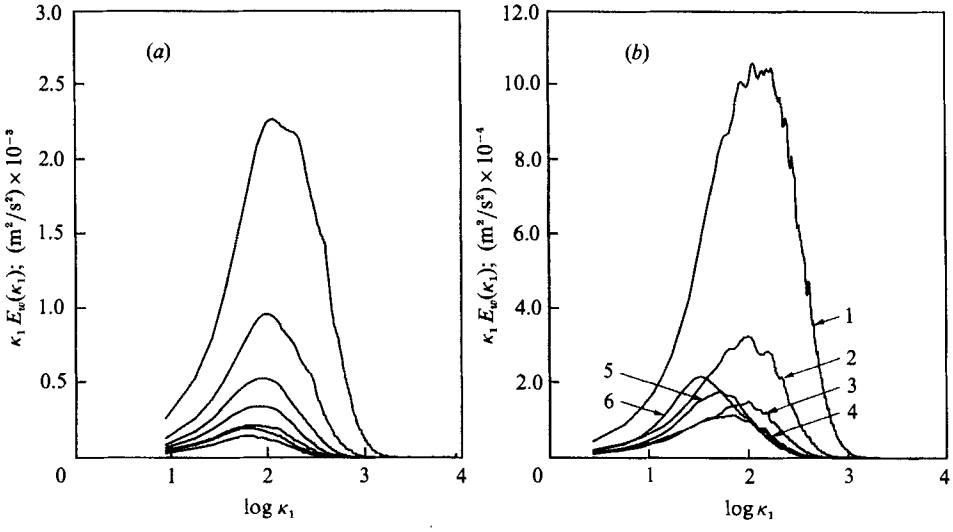

FIGURE 5. The evolution of the vertical velocity spectra; $\kappa_1 E_w(\kappa_1)$ *vs.* $\log \kappa_1$. (*a*) $Fr_M = 253$. The x/M locations are 36.5, 76.5, 116.5, 156.5, 196.5, 236.5 and 276.5. (The peak of the curve decreases with x/M.) (*b*) $Fr_M = 84.8$; $x/M = 36.5$ (1), 76.5 (2), 116.5 (3), 156.5 (4), 196.5 (5) and 236.5 (6).

Finally, for this case too the variance decreases. A similar oscillatory effect where kinetic and potential energy are exchanged has been shown in the numerical simulations of Riley *et al.* (1981). The above trends were observed by LV although they did not observe the interesting case in which the vertical velocity variance increases, as for our most stable case.

The striking increase in the vertical velocity variance for the most stable case is evident when its spectra are contrasted with a weakly stratified case, figure 5. Here we have plotted $\kappa_1 E_w(\kappa_1)$ where $E_w(\kappa_1)$ is the vertical velocity spectrum defined such that

$$\int_0^\infty E_w(\kappa_1)\,\mathrm{d}\kappa_1 = \overline{w^2}$$

and κ_1 is the wavenumber in the longitudinal direction. The magnitude of the curve indicates the energy at that particular wavenumber. The peak of these spectra may be viewed as an approximate measure of the integral scale (Lumley & Panofsky 1964). Notice that while for the weakly stable case (figure 5*a*) there is a monotonic decrease in the magnitude of the spectra with downstream distance, for the active case (figure 5*b*) the spectra first decrease and then increase with downstream distance. In both cases the peak shifts to lower wavenumbers (as they must in grid turbulence) although the shift is greater for the strongly stratified case. (This will be discussed further below when we examine the evolution of the lengthscales.) Note also that the width of the spectra do not appear to be significantly affected by the stratification; figure 5(*b*) suggests that as the vertical kinetic energy budget is replenished from the potential energy it occurs at all wavenumbers. This is also confirmed by normalizing the spectra of figure 5 by the variance (equal area plots, not shown here) although strict comparison is not possible since the flow speeds were different ($U = 3.5$ m/s, $Fr_M = 253$; $U = 2.8$ m/s, $Fr_M = 84.8$) and so the spectra for the weakly stratified case should be slightly broader because it has a higher turbulence Reynolds number (table 1).

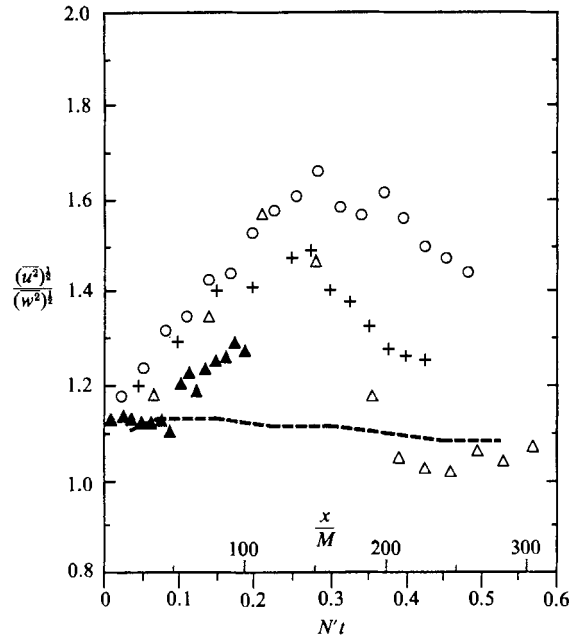

FIGURE 6. The ratio of the intensity of the velocity fluctuations $((\overline{u^2})^{\frac{1}{2}}/(\overline{w^2})^{\frac{1}{2}})$ as a function of $N't$. △, $Fr_M = 84.8$; ○, $Fr_M = 114$; +, $Fr_M = 127$; ▲, $Fr_M = 253$; ------, passive data (as a function of x/M).

Figure 6 shows a plot of the ratio of the longitudinal to vertical r.m.s. velocity fluctuations $(\overline{u^2})^{\frac{1}{2}}/(\overline{w^2})^{\frac{1}{2}}$, from here on referred to as I_{uw}. We have plotted I_{uw} as a function of $N't$ for the active case and as a function of x/M for the passive case (where $N' = 0$). We have adjusted the two scales such that $N't = x/M$ for the most active case ($Fr_M = 84.8$), i.e. for this case either scale may be used (for the higher Fr_M cases the tunnel is shorter in terms of $N't$, but the measurements were all carried out to the same downstream extent). This plotting procedure allows us to compare the active and passive cases and will be used again in figure 8. For the passive case I_{uw} is a little greater than 1.1 and slowly decreases with downstream distance, in accord with previous workers (Comte-Bellot & Corrsin 1966). For the active cases I_{uw} increases as the buoyancy extracts energy mainly from the vertical kinetic energy component. The ratio then tends to unity as the velocity variance decay is attenuated (figure 4). We will show below that at this latter stage the vertical heat flux has been destroyed by the stratification. Notice that for the highest stability case ($Fr_M = 84.8$) the I_{uw} attains a value of unity far downstream. We also note that I_{uw} is frequently used as an indicator of the anisotropy of the turbulence (Comte-Bellot & Corrsin 1966) with a value of unity indicating isotropy. However, for the flow described here, with multiple lengthscales and the possible existence of gravity waves, little can be inferred about the isotropy from I_{uw}. Indeed we will show below that the ratio of the vertical to longitudinal lengthscale obtained from the spectra indicate the flow is not isotropic in the region far downstream where I_{uw} approaches unity.

As discussed in §2, there are a number of ways of defining turbulence integral scales and these are shown in figure 7. Figure 7(*a*) shows the evolution of the longitudinal and transverse integral scales L_f and L_g respectively, for the active and passive cases. To determine L_f the auto-correlation function of u was integrated

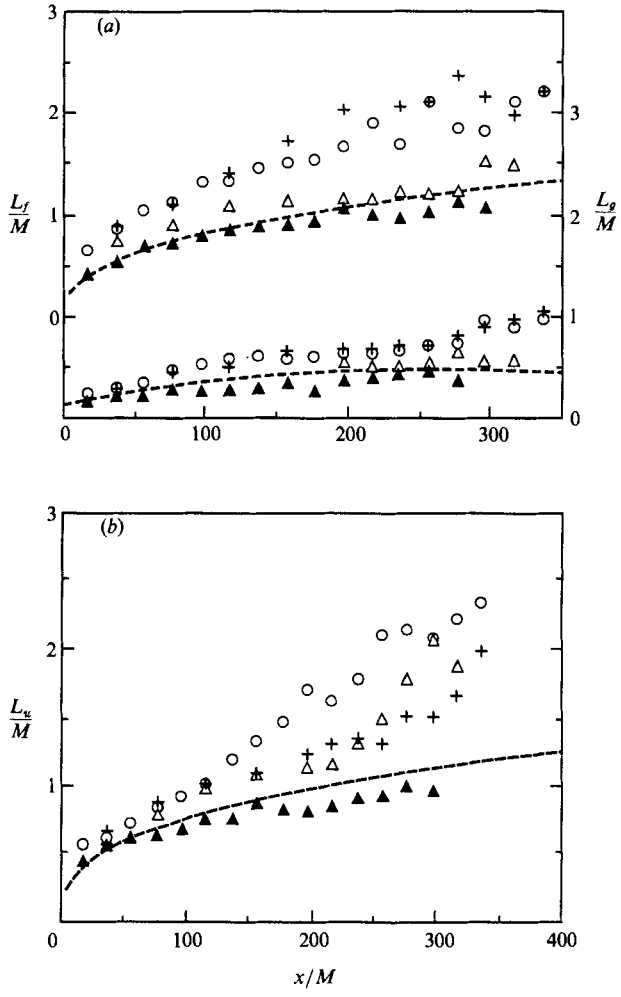

FIGURE 7. The evolution of the integral scales. (*a*) L_f/M (longitudinal integral scale) and L_g/M (transverse integral scale). The lower curve is L_g/M (right-hand scale). △, $Fr_M = 84.8$; ○, $Fr_M = 114$; +, $Fr_M = 127$; ▲, $Fr_M = 253$; ------, best fit for passive data. (*b*) L_u/M ($L_u = (\overline{u^2})^{\frac{3}{2}}/\epsilon$), symbols are the same as in (*a*).

up to its first zero crossing and Taylor's hypothesis was used to convert time to length: $L_f = U\mathscr{I}_f$ where $\mathscr{I}_f$ is the integral of the auto-correlation function. The same procedure was followed for L_g using the w time series, except here the auto-correlation function was integrated to its second zero crossing (Comte-Bellot & Corrsin 1971). Although there is considerable scatter, figure 7 (*a*) shows that L_f tends to be greater for the active than passive cases excepting for the most stable case ($Fr_M = 84.8$) where it tends towards the passive value as the flow evolves. L_g (also shown in figure 7*a*) appears to behave similarly to L_f. Figure 7 (*b*) shows the evolution of $L_u \equiv (\overline{u^2})^{\frac{3}{2}}/\epsilon$. While its broad trend is similar to L_f notice that here the data for the active cases is initially closer to the passive line (up until $x/M \approx 80$) than it was for L_f. L_u then departs from the passive line and becomes larger as the effects of the stratification become more pronounced. Note also that as for L_f, L_u for the most stable case ($Fr_M = 84.8$) is closest to the passive value except near the end of the

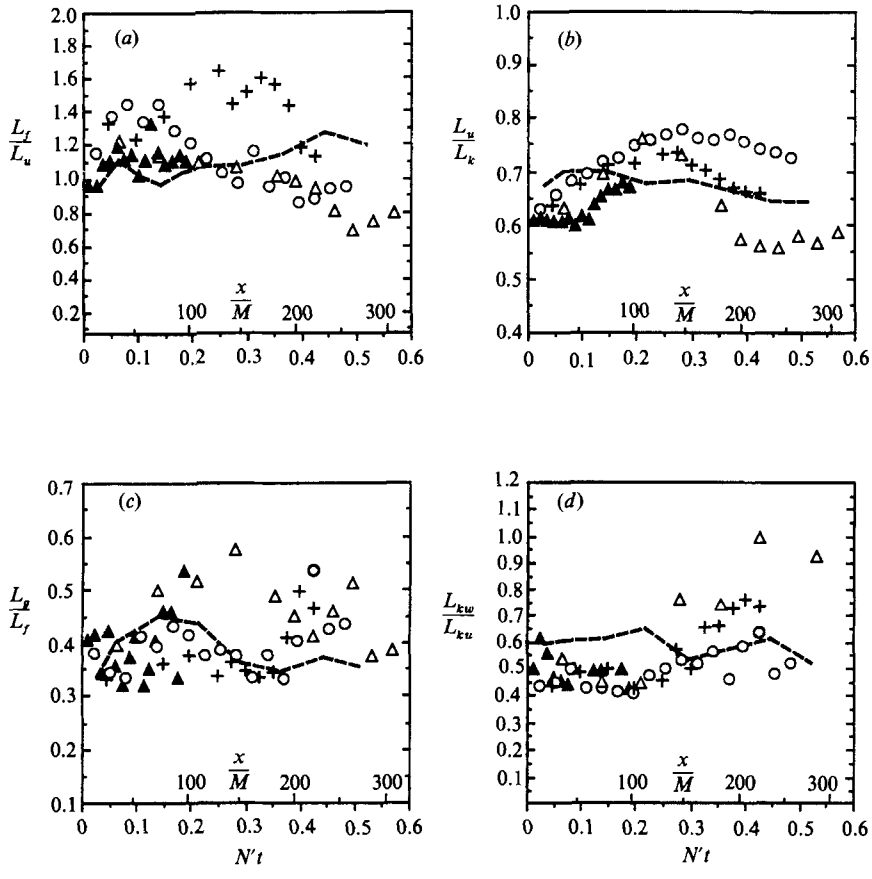

FIGURE 8. Evolution of the ratio of integral lengthscales. (*a*) L_f/L_u; (*b*) L_u/L_k; (*c*) L_g/L_f; (*d*) L_{kw}/L_{ku} (the ratio of the (inverse) peak of the vertical velocity spectrum to the (inverse) peak of the horizontal velocity spectrum). Symbols are the same as figure 7. Line is for the passive case (plotted as a function of x/M).

tunnel ($x/M > 200$) where there is a departure (this may also be observed, but to a much less extent, in the last two points of L_f (figure 7*a*)). As stated in the introduction, when we refer to 'the integral scale' it will be to L_u (often to be written as L) since we believe its value is better conditioned than L_f.

Figure 8 shows ratios of various integral scales. The ratio L_f/L_u (figure 8*a*) tends initially to be greater than for the passive case and then falls below it but there is much scatter. The essential point is that the ratio is always close to unity. The ratio L_u/L_k (figure 8(*b*), where $L_k \equiv \overline{k^2}^{\frac{3}{2}}/\epsilon$) also does not depart substantially from the passive value. Note for isotropic turbulence ($\overline{u^2} = \overline{v^2} = \overline{w^2}$) its value is 0.543. (In passive grid turbulence $\overline{v^2} = \overline{w^2} < \overline{u^2}$ and its value is around 0.65). Figure 8(*c*) shows the ratio of the longitudinal integral scale to the transverse integral scale. There is much scatter but there is a tendency for L_g/L_f, for the stratified data, to have a value greater than that of the passive value (0.4) as the flow evolves. Finally figure 8(*d*) shows the ratio of lengthscales determined from the (inverse) wavenumber peak of the one dimensional energy spectra such as from those shown in figure 5. Here, too, there is much scatter but there seems to be a significant departure from the passive value for the most stable case for $N't > 0.3$ ($x/M > 150$). In this region the vertical

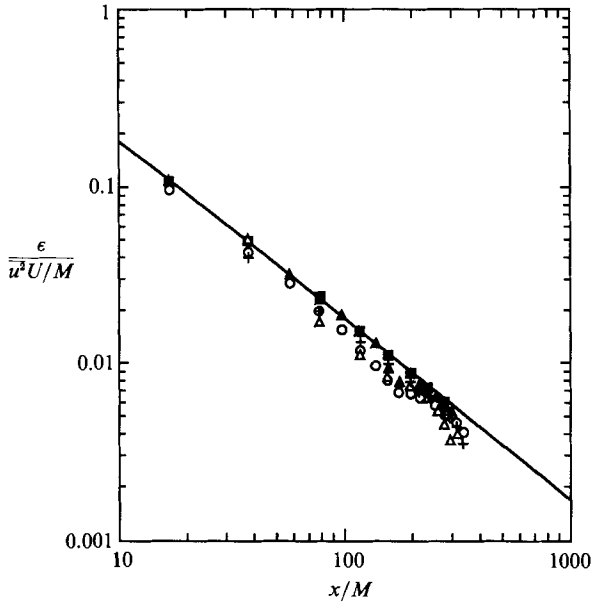

FIGURE 9. The dissipation rate of the turbulent kinetic energy, $\epsilon/(\overline{u^2}U/M)$. Symbols are the same as figure 4.

lengthscale is enhanced relative to the longitudinal lengthscale. As already noted, a suggestion of this is also found in figure 8(*c*). It appears, then, that when the stored potential energy is being fed back to the vertical component of kinetic energy (xM) > 150, figure 4), the vertical lengthscale becomes larger than that of the streamwise lengthscale. Notice that in this region the ratio of the intensities of the u- and v-components tends towards unity (figure 6). The fact that energy is being fed back into the w-component at larger scales than those of the longitudinal component, far downstream ($Nt > 0.3$), may be suggestive of wave motion although, as will be shown below, there is no strong evidence of waves in the cross spectra. On the other hand, it does not appear, from the spectra or correlation functions, for the region $Nt < 0.3$ (where the vertical fluctuations are decaying more rapidly than for the neutral case (figure 4) and I_{uv} is increasing (figure 6)), that the transverse scale is significantly reduced relative to the longitudinal lengthscale (as would be expected) although L_{kw}/L_{ku} is slightly smaller than for the passive case (figure 8*d*).

Figure 9 shows the non-dimensional dissipation rate of the turbulent kinetic energy. The dissipation rate was determined for the active cases from the two dissipation spectra as follows:

$$\epsilon = 10\nu \int_0^\infty E_{u,x}(\kappa_1)\,\mathrm{d}\kappa_1 + 2.5\nu \int_0^\infty E_{w,x}(\kappa_1)\,\mathrm{d}\kappa_1.$$

($E_{u,x}$ and $E_{w,x}$ are the spectra of $\partial u/\partial x$ and $\partial w/\partial x$ respectively. We have transformed the derivative time series using Taylor's hypothesis.) Here, following Stillinger *et al.* (1983*b*), we have assumed that $\overline{v^2} = \overline{u^2} > \overline{w^2}$ although the results are within a few per cent of those obtained assuming isotropy (Yoon 1989). For the passive case the relation $\epsilon = -\mathrm{d}k/\mathrm{d}t$ where $k = \frac{1}{2}(\overline{u^2} + 2\overline{w^2})$ was used since here $\overline{w^2} = \overline{v^2} < \overline{u^2}$. We also confirmed that this estimate was within a few per cent of the value obtained from the spectra. A passive normalization has been used in figure 9 in order to observe how the

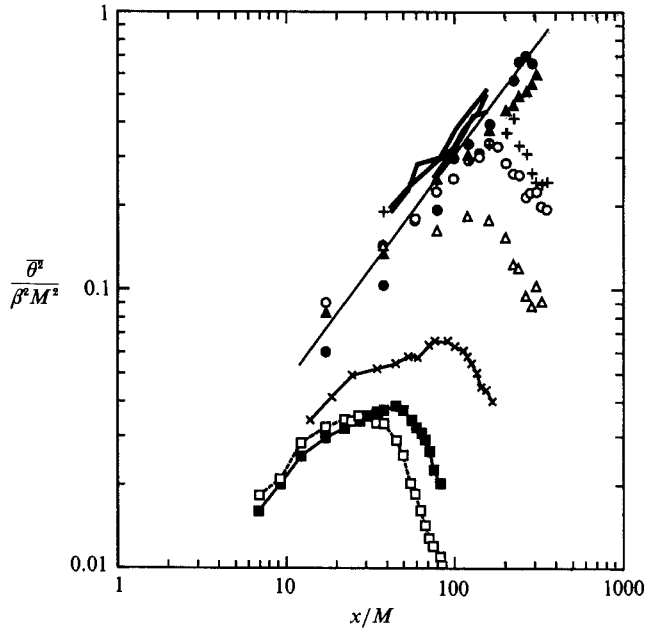

FIGURE 10. The evolution of the normalized temperature variance, $\overline{\theta^2}/\beta^2M^2$. △, $Fr_M = 84.8$; ○, $Fr_M = 114$; +, $Fr_M = 127$; ●, $Fr_M = 192$; ▲, $Fr_M = 253$; ——, passive data (Sirivat & Warhaft 1983). The three data sets from Lienhard & Van Atta are: □, $Fr_M = 17.1$; ■, $Fr_M = 22$; ×, $Fr_M = 48.1$. (The first two of these are for a two-inch grid and the third is for a one-inch grid.) The line has a slope of -0.7 (see text).

active case departs from the passive (Lienhard 1988; Yoon 1989). For the passive case, assuming isotropy, $\epsilon/(\overline{u^2}U/M) = \frac{3}{2}n(x/M)^{-1}$. The straight line in figure 9 has a slope of -1. Notice there is a small but significant departure for the active cases showing that the rate of dissipation is reduced by the buoyancy. This was also observed by LV. We will compare the dissipation rate to the other terms in the energy budget in §4 below.

4.2. *The temperature variance and heat flux*

The evolution of the temperature variance and heat flux for a passive linear temperature profile in grid turbulence was dealt with in detail by Sirivat & Warhaft (1983). Figure 10 summarizes the temperature variance results for that previous study and includes the present results both for a passive gradient and for various degrees of stable thermal stratification. Also included in the figure are some results of LV. We have plotted the data against x/M in order to contrast the active and passive cases and to emphasize differences in the work of LV and our own. The temperature variance has been normalized by β^2M^2. This passive normalization results from solving equation (3) (for $\overline{\theta^2}$), assuming a power law decay for the velocity variance ($\overline{u^2}/\overline{U^2} \propto (x/M)^{-n}$) and that the mechanical to thermal timescale ratio is unity, i.e. $\epsilon_\theta \propto \overline{\theta^2}/\tau$. Using this procedure (Sirivat & Warhaft 1983; Yoon 1989) the solution of equation (3) is: $\overline{\theta^2}/(\beta^2M^2) = C(x/M)^{2-n}$ where the constant C is determined by the initial intensity of the thermal and velocity fluctuations. Thus for $n = 1.3$, the slope for the passive line should be 0.7: the best-fit line shown in the figure has a slope of 0.8 indicating that the assumptions are reasonable. We will describe ways of collapsing the active data in §4.

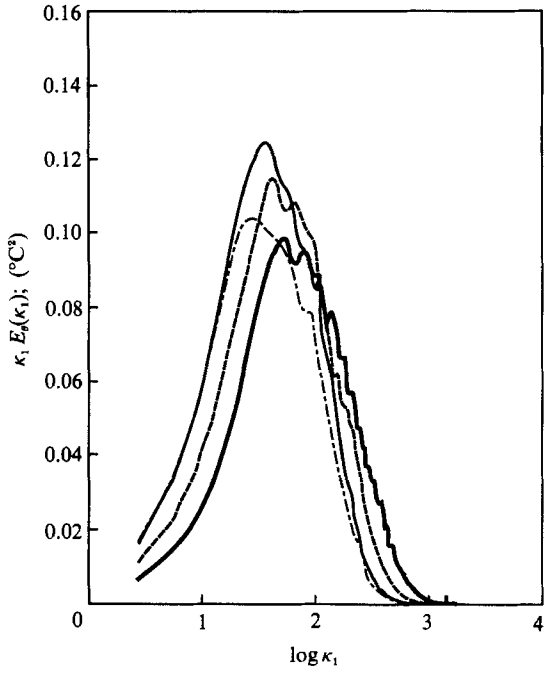

FIGURE 11. The evolution of the temperature spectra, $\kappa_1 E_\theta(\kappa_1)$ *vs.* $\log \kappa_1$. $Fr_M = 84.8$ ——, $x/M = 36.5$; – – –, $x/M = 76.5$; ——, $x/M = 116.5$; – · – · –, $x/M = 196.5$.

Figure 10 clearly shows the effects of the thermal stability on the evolution of $\overline{\theta^2}$. As N is increased $\overline{\theta^2}$ begins to depart from the passive line at earlier non-dimensional downstream distances. The variance peaks and then rapidly decays as its production term ($-\overline{\theta w}\beta$, equation (3)) is diminished by the stratification (the evolution of the heat flux is discussed below, see figure 14). Notice that for the data of LV the departure from the passive case occurs as early as $x/M = 20$, i.e. before the turbulent wakes from the grid have become isotropic and the velocity power law decay is established (Comte-Bellot & Corrsin 1966). We will discuss this aspect in more detail below. Notice too that the data set of LV is shifted to the right of our passive line. This is due to the differences in the intensity of the velocity decay for the two experiments and will also be addressed in §5.

The one-dimensional temperature spectrum $E_\theta(\kappa_1)$ (where $\int_0^\infty E_\theta(\kappa_1)\,d\kappa_1 = \overline{\theta^2}$) is plotted in figure 11 for the most stable case ($Fr_M = 84.8$). As for the vertical velocity spectra (figure 5) we have multiplied $E_\theta(\kappa_1)$ by κ_1 in order to provide an 'energy' plot. The magnitude of the peak varies with downstream distance, first increasing and then decreasing in the same way as the temperature variance. Notice that the width of the spectrum does not appear to decrease significantly as the flow evolves and the stratification effects become more dominant.

Figure 12 shows the evolution of the temperature integral scale, L_T, derived from the temperature auto-correlation function in the same way as L_f. As for L_f (figure 7), L_T also appears to increase relative to the passive case as the buoyancy effects become more pronounced. Notice, however, that for the strongest stability ($Fr_M = 84.8$) L_T starts to decrease in the region where the vertical kinetic energy is being provided with energy from the potential energy field ($x/M \approx 200$, see figure 4). Figure 12(*b*) shows the ratio of L_T/L_f. There is much scatter but the plot, as a function of

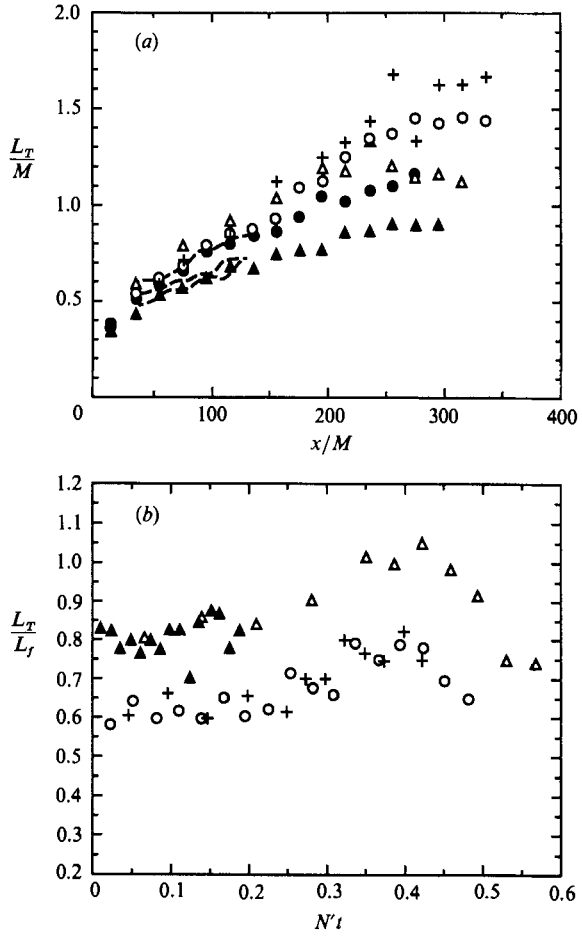

FIGURE 12. The temperature integral lengthscale, L_T derived from the auto correlation function. (*a*) L_T/M *vs.* x/M. Symbols are the same as for figure 10. The dashed line is for the passive case (Sirivat & Warhaft 1983). (*b*) L_T/L_f *vs.* $N't$. Symbols are the same as in (*a*).

$N't$, shows a small maximum for the three most stable cases at $N't \approx 0.4$. Sirivat & Warhaft (1983) found that for the passive case $L_T/L_f \approx 0.8$ and remained relatively constant as the flow evolved, although in that case too there was much scatter in the data. It appears, then, that the buoyancy does not have a pronounced effect on this ratio.

The destruction rate of $\overline{\theta^2}$, ϵ_θ, is shown in figure 13 using a passive normalization procedure similar to that used for $\overline{\theta^2}$. ϵ_θ was determined from the temperature spectra using the relation $\epsilon_\theta = 3\alpha \int_0^\infty E_{\theta,x}\, \mathrm{d}\kappa_1$ where α is the thermal diffusivity and $E_{\theta,x}$ is the spectrum of $\partial\theta/\partial x$ (as for the calculation of ϵ, Taylor's hypothesis has been used). Both our data and that of LV collapse well on a log–log plot with $N't$ as the abscissa. The break in the curve from the essentially passive state ($\epsilon_\theta \propto t^{1-n}, n \approx 1.33$) occurs at $N't \approx 0.2$ where the decay exponent increases to approximately -2. This is at the peak of the temperature variance curve, i.e. the point where advection term in the $\overline{\theta^2}$ equation (left-hand term in equation (3)) changes sign due to the collapse of the vertical heat flux, which will now be addressed.

The ability of stable stratification to inhibit turbulent mixing is most clearly

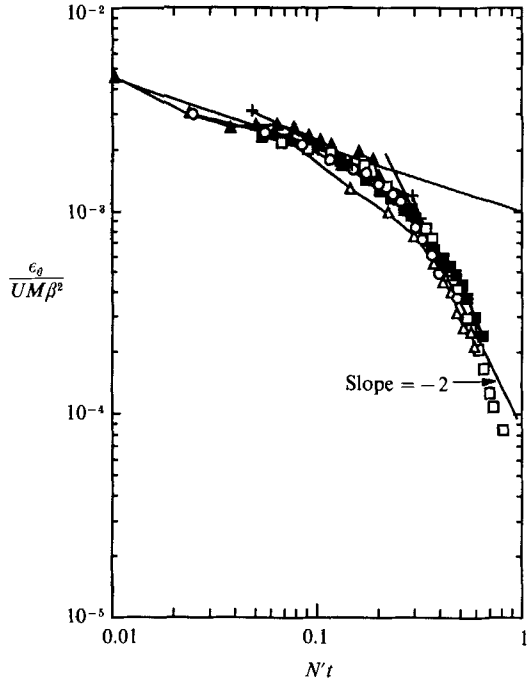

FIGURE 13. The evolution of the normalized destruction rate of temperature variance, $\epsilon_\theta/(UM\beta^2)$. Symbols are the same as for figure 10.

manifest in the evolution of the vertical convective heat flux,† $\rho_0 C_p \overline{w\theta}$, which is shown in figure 14(*a*) normalized by the molecular heat flux $-K\beta$ (which is constant). Here C_p and K are respectively the specific heat at a constant pressure and thermal conductivity of the air. The difference between our data and that of LV (also plotted) will be discussed in a moment. Here we note the qualitative agreement between the two data sets. By $N't \approx 0.3$ the vertical heat flux is close to zero and, for the most stable case ($Fr_M = 84.8$), there is a small but significant region in which there is a counter gradient heat flux. It is more illuminating to examine the correlation coefficient of the kinematic heat flux $\rho_{w\theta} \equiv \overline{w\theta}/((\overline{\theta^2})^{\frac{1}{2}}(\overline{w^2})^{\frac{1}{2}})$ which is plotted in figure 14(*b*). Although here, too (apart from the counter heat flux case) there is broad qualitative agreement with LV, their data are shifted by about $0.15N't$ to the right of our set. Clearly plotting $\rho_{w\theta}$ as a function of $N't$ does not collapse the data of the two experiments. The reason for this will be given in the next section. However, within each experiment, the data for various N collapse well when plotted against this form of non-dimensional time. (An exception to this is the counter-gradient heat flux case which only collapses with the rest of the data until $N't \approx 0.3$. The reason for the bifurcation at $N't \approx 0.3$ as the stability increased is unclear. It will be discussed further below.) Note that the non-dimensional time between the point where the correlation coefficient begins to decay and its maximum value is about 0.3

† Hunt (1985) and Pearson, Puttock & Hunt (1983) show that from a Lagrangian viewpoint the vertical heat flux has two components: the first caused by the growth of the displacements of fluid elements and the second caused by the mixing between fluid elements. They argue that in strongly stably stratified flows most of the heat flux is caused by the second mechanism, i.e. by fluid elements exchanging temperature during their bounded oscillations. Unfortunately our Eulerian measurements are unable to separate these two effects.

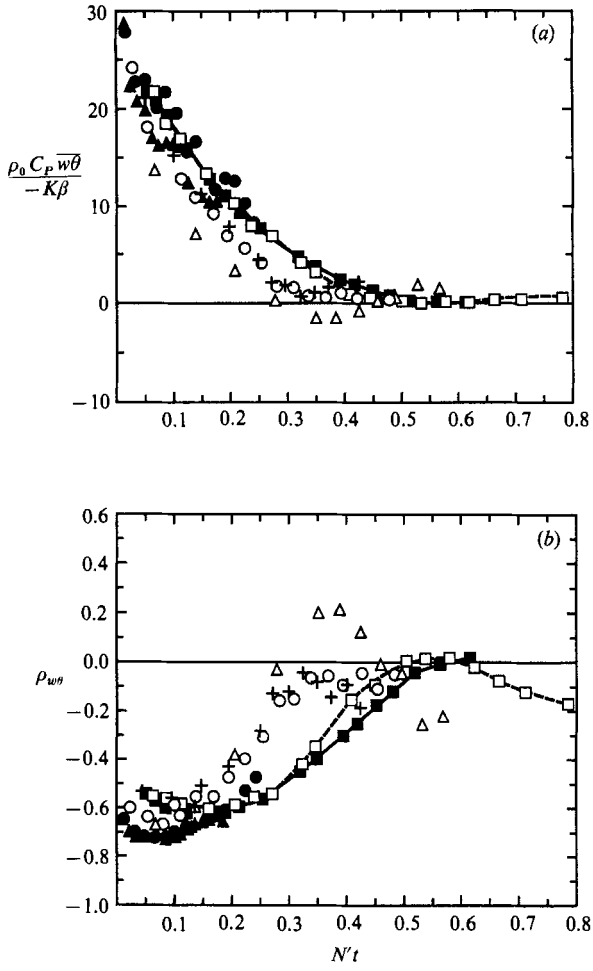

FIGURE 14. The heat flux. (*a*) The ratio of the vertical turbulent heat flux ($\rho_0 C_p \overline{w\theta}$) to the molecular heat flux ($-K\beta$). (*b*) The cross-correlation coefficient $\rho_{w\theta} = \overline{\theta w}/((\overline{\theta^2})^{\frac{1}{2}}(\overline{w^2})^{\frac{1}{2}})$. Symbols are the same as in figure 10.

and is approximately the same for each data set. There are two other differences in the data sets. First, for small $N't$ (the approximately passive region) our value of $\rho_{w\theta}$ is -0.7 compared to -0.6 for LV. Sirivat & Warhaft found $\rho_{w\theta} = -0.7$ for their passive experiments, and Budwig *et al.* (1985) found a value between -0.7 and -0.8, but less negative values have been observed by other workers (e.g. Venkataramani & Chevray 1978). Secondly, and more significantly, for our strongest stratification there is a pronounced region of counter gradient heat flux where $\rho_{w\theta}$ reaches a value of 0.25, a result that was repeatable from further trials using the same initial conditions. There is no comparable region where the net heat flux is counter to the gradient in the experiment of LV. Regions of counter-gradient heat flux were observed, however, in the salt-water experiments of Stillinger *et al.* (1983*a*, *b*) and Itsweire *et al.* (1986). Note that for the counter-gradient case observed here the peak of $\rho_{w\theta}$ occurs at approximately the same value of $N't$ (≈ 0.35) as the peaks for our other stable cases shown.

Figure 15 shows the co-spectra for a weakly stratified case ($Fr_M = 253$) and the

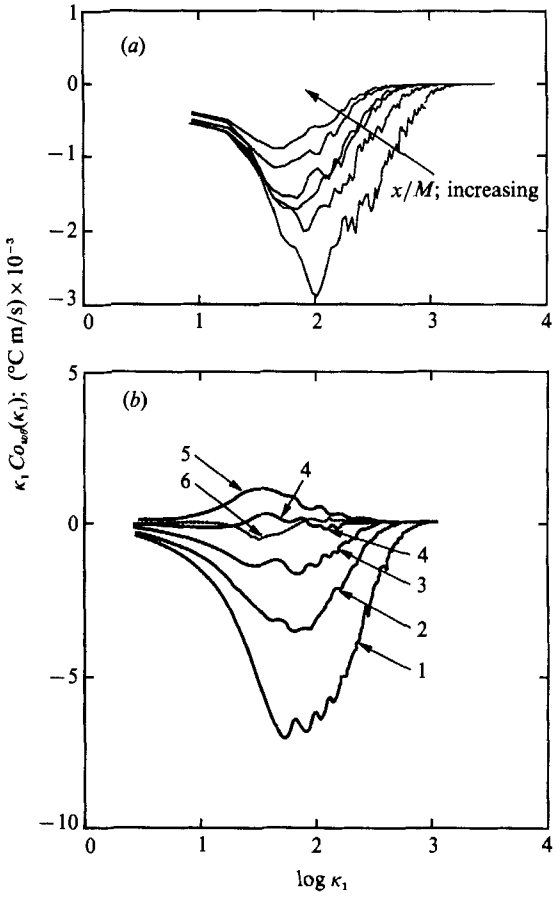

FIGURE 15. The evolution of the co-spectra of the kinematic heat flux. ($\kappa_1 Co_{w\theta}(\kappa_1)$ *vs.* $\log \kappa_1$) (*a*) $Fr_M = 253$, $x/M = 16.5$, 36.5, 56.5, 76.5, 116.5, 156.5, 196.5 (*b*) $Fr_M = 84.8$; $x/M = 36.5$ (1); 76.5 (2); 116.5 (3); 156.5 (4); 196.5 (5); 236.5 (6).

case where the counter heat flux occurs ($Fr_M = 84.8$). For the former case the magnitude of the co-spectrum diminishes with downstream distance, mainly because of the reduction in the vertical velocity and temperature variances (the cross correlation coefficient remains essentially constant for this case (figure 14). However, for the strongly stratified case the co-spectrum reverses sign, first at the lower wavenumbers ($x/M = 156.5$) and then at all wavenumbers ($x/M = 196.5$) causing a net counter gradient heat flux (figure 14). Finally as $\rho_{w\theta}$ comes to its second zero crossing (figure 14) the low wavenumber end of the co-spectrum becomes negative again.

The distribution of the phase angle between w and θ, $Ph_{w\theta}$, as a function of wavenumber, is shown in figure 16, for the most stable case (with the countergradient heat flux). $Ph_{w\theta}$ was determined from the one-sided cross spectral density function, $G_{w\theta}(\kappa_1) = C_{w\theta}(\kappa_1) - jQ_{w\theta}(\kappa_1)$, where $C_{w\theta}(\kappa_1)$ and $Q_{w\theta}(\kappa_1)$ are the co- and quadrature-spectra, respectively. The phase of this complex function is defined such that $\tan Ph_{w\theta} = -Q_{w\theta}(\kappa_1)/C_{w\theta}(\kappa_1)$. In this work we have taken $Ph_{w\theta} = +180°$ when w and θ are out of phase by 180 ° (although $-180°$ is equally accepatble). $C_{w\theta}(\kappa_1)$ and $Q_{w\theta}(\kappa_1)$ were determined using standard FFT procedures (Bendat & Piersol 1971). Early

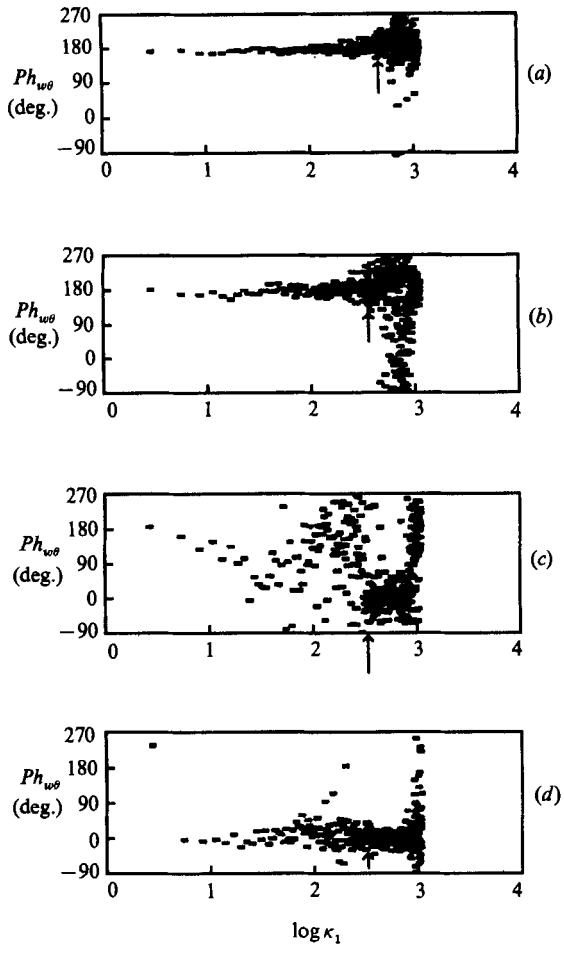

FIGURE 16. The phase angle between w and θ as a function of wavenumber. $Fr_M = 84.8$. (*a*) $x/M = 76.5$; (*b*) $x/M = 116.5$; (*c*) $x/M = 156.5$; (*d*) $x/M = 196.5$. The vertical arrow is when the co-spectrum is approximately zero, to its right is noise.

in the flow development $Ph_{w\theta}$, is 180° across the whole wavenumber range. Here the turbulent heat flux is down the gradient, i.e. a negative (downward) fluctuation in w is associated with a positive temperature fluctuation. Thus w and θ are anti-correlated (180° out of phase) and the quadrature spectrum is essentially zero. A value of $Ph_{w\theta} \approx 180°$ was also observed for the passive case (Yoon 1989), but here it remained at 180° for all downstream locations (as would be expected). For (down gradient) turbulent heat transport to occur w and θ must be predominantly 180° out of phase since by definition

$$\overline{w\theta} = \int_0^\infty C_{w\theta}(\kappa_1)$$

and the quadrature spectrum does not contribute to the heat flux. When the heat flux begins to collapse, $Ph_{w\theta}$ appears to be scattered between 0° and 180° in the energy containing range of the co-spectrum (figure 16*c*). Finally for the counter-gradient region w and θ are essentially in phase across the whole spectrum ($Ph_{w\theta} \approx 0°$,

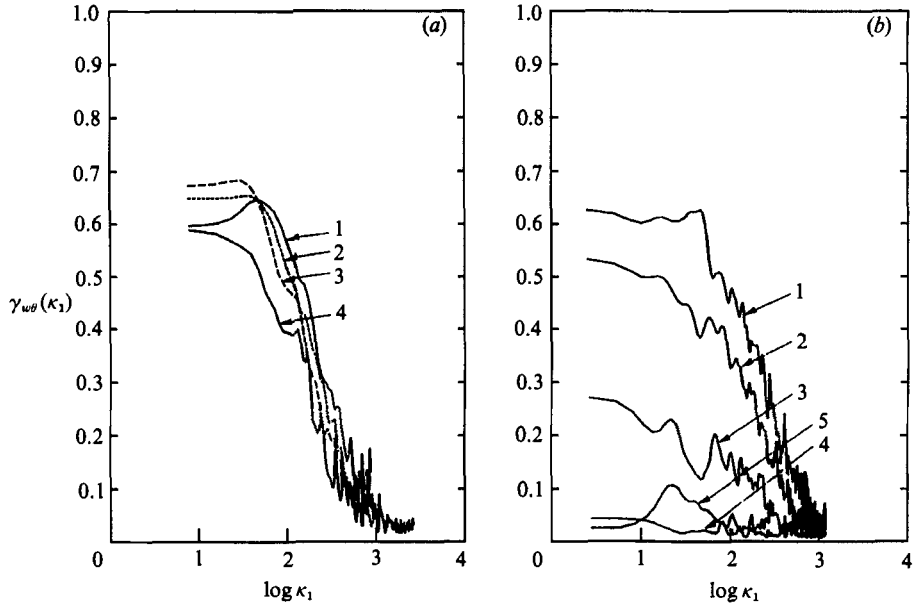

FIGURE 17. The evolution of the coherence between w and θ as a function of wavenumber. (a) $Fr_M = 253$: $x/M = 36.5$ (1); 76.5 (2); 116.5 (3); 196.5 (4). (b) $Fr_M = 84.8$; $x/M = 36.5$ (1); 76.5 (2); 116.5 (3); 156.5 (4); 196.5 (5).

figure 16(d). There does not appear to be any significant wavenumber region where $Ph_{w\theta} = 90°$ during the evolution of the heat flux, a value indicative of random internal wave motion. As discussed by Stewart (1969) and used as a diagnostic tool by Axford (1971), Caughey (1977), Hunt, Kaimal & Gaynor (1985) and others, internal gravity waves should, if present, produce a large quadrature spectrum but a small co-spectrum for θ and w; i.e. there should be no transport of heat by the wave motion and $Ph_{w\theta} \approx 90°$. (Consider a pure sinusoidal disturbance of w and θ in a stratified medium with no mixing.) Presumably internal waves do exist since there is significant potential energy in the flow when the heat flux has collapsed (see §5) but they are either masked by the active turbulence or, single-point measurements are insufficient to detect them. For the other strongly stratified cases the evolution of the phase spectrum (not shown) followed the sequence of figure 16(a–c) but then remained scattered as in figure 16(c) until the end of the tunnel. For these cases a counter gradient heat flux was not observed. LV do not find significant regions in which $Ph_{w\theta} \approx 90°$ for their stratified experiments either.

The lack of evidence of internal waves is further borne out by the coherence measurements, figure 17. The coherence $\gamma^2_{w\theta}(\kappa_1) \equiv (Co^2_{w\theta}(\kappa_1) + Q^2_{w\theta}(\kappa_1))/E_w(\kappa_1)E_\theta(\kappa_1)$ provides wavenumber information on the correlation between w and θ. If waves were present a strong coherence should be observed even in the absence of a heat flux. Figure 17(a) shows that for the weakly stratified case, the coherence is high in the energy containing region and this is consistent with the strong turbulent vertical heat flux. For the most stable case, figure 17(b), the coherence collapses with the heat flux and there is no wavenumber band with significant coherence when the heat flux decays to zero (a small coherence is observed with the counter gradient heat flux).

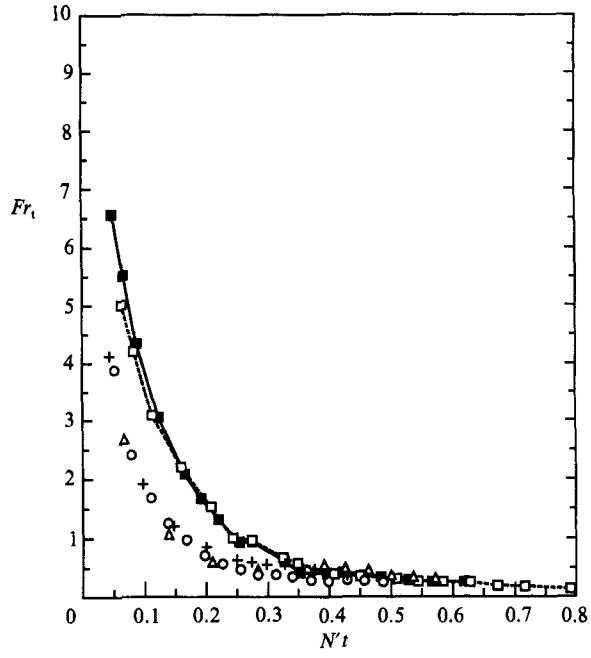

FIGURE 18. The turbulent Froude number $Fr_t (= L_b/L)$ *vs.* $N't$. Symbols are the same as in figure 10.

5. Discussion of the results

We will now discuss the results presented in §4 in terms of length, time and other relevant dimensionless ratios. We will contrast different methods of scaling the data noting that we have two objectives: first to provide a coherent picture of our own experiment and secondly to relate our results to those of previous work, both experimental and numerical.

Figure 18 shows the variation of the turbulent Froude number $Fr_t = L_b/L$ $(= (\overline{w^2})^{\frac{1}{2}}/NL)$ as a function of $N't$. The rapid decay reflects, of course, the approximate power law decay of $\overline{w^2}$ (figure 4). If we use the heat flux correlation coefficient $\rho_{w\theta}$ (figure 14*b*) as an approximate guide as to the change in flow dynamics with stability (noting that $\rho_{w\theta} \approx$ constant ≈ -0.7 for the passive case) then it appears that the transition from passive to stably stratified turbulence occurs at $N't \approx 0.08$, since this is when $\rho_{w\theta}$ begins to decrease in magnitude. This corresponds to $Fr_t \approx 2$ in figure 18. By the time the heat flux has collapsed (or become counter gradient) at $N't \approx 0.3$, $Fr_t \approx 0.3$. Approximately the same transition Froude number (≈ 2) is seen in the data of LV since $\rho_{w\theta}$ for their data does not begin to decay until $N't \approx 0.15$.

The plot of L_b/L_θ (figure 19) shows that significant buoyancy effects occur when this ratio is approximately 4 (and slightly less than 4 for LV); again we are using the evolution of $\rho_{w\theta}$ as the criterion for the onset of buoyancy. Since $(L_\theta/L_b)^2$ is the ratio of potential energy to vertical kinetic energy (equation (7)) it is evident that buoyancy begins to play a significant role when the fluctuating potential energy is around 5% ($(L_\theta/L_b)^2 \approx 0.05$ when $N't \approx 0.08$) of the fluctuating vertical kinetic energy. Both curves decline to minimum values, unity for LV (occurring at $N't \approx 0.45$) and approximately 1.2 for the present work (at $N't \approx 0.3$). Thus for LV the

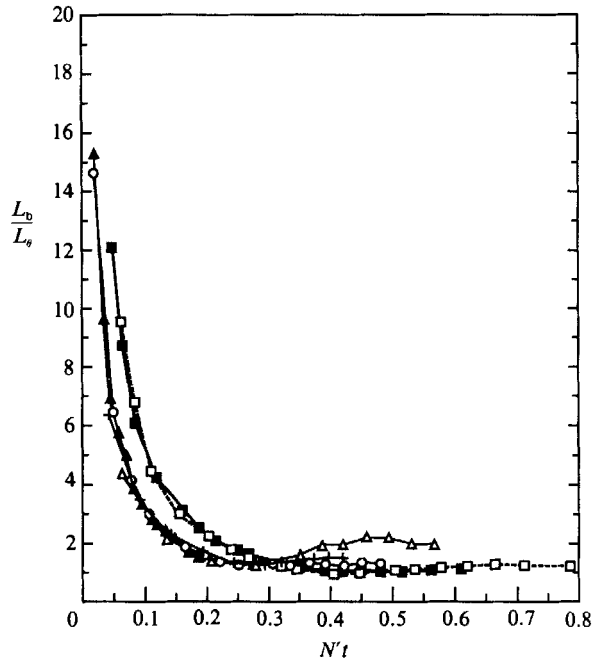

FIGURE 19. The ratio of the buoyancy to overturning lengthscale, L_b/L_θ *vs.* $N't$. Symbols are the same as in figure 10.

potential and vertical kinetic energy are equal at this stage (where the heat flux has collapsed). Our data, on the other hand, shows that, even for the most stable case, the vertical kinetic energy is always greater than the potential energy. The actual values of fluctuating total turbulent kinetic energy, vertical kinetic energy and potential energy are shown in figure 20 for two of our experiments, $Fr_M = 84.8$ and 114. Notice (figure 19) the oscillation of L_b/L_θ for the most stable case ($Fr_M = 86.4$) in the region where the counter heat flux occurs (figure 14). The peak value is at $N't \approx 0.45$.

The results of figures 19 and 20 compare favourably with the numerical simulations of Riley *et al.* (1981) done for $N = 1.57$, a value close to our most stable case of $N = 1.3$; $Fr_M = 84.8$. As for our experiment Riley *et al.* find the potential energy peaks (when L_b/L_θ is at a minimum) at approximately $\frac{1}{4}$ the Brunt–Väisälä period and the vertical kinetic energy has its first peak at around $N't \approx 0.5$ (when L_b/L_θ is at a maximum). The numerical simulations also show a similar region of counter gradient heat flux to our experiment. Finally, Riley *et al.* find, as we do, that the fluctuating potential energy is always less than the vertical kinetic energy, i.e. $L_b/l_\theta > 1$. On the other hand, Métais (1987), using initial conditions taken from the salt-water experiments of Itsweire *et al.* (1986) (but using a Prandtl number of unity), finds, in accordance with the salt-water experiments, that $L_b/L_\theta < 1$ for a significant extent of the evolution of his numerical solutions.

Figure 21 shows two more lengthscale ratios, L_{DO}/L_b and L_θ/L_u. The ratio of the Dougherty–Ozmidov lengthscale L_{DO} to the buoyancy lengthscale L_b has been shown in the introduction to be approximately equal to $Fr_t^{\frac{1}{2}}$ and this is evident if figure 21 (*a*) is compared with figure 18. The ratio of the overturning lengthscale to the integral lengthscale (figure 21 *b*) tends to increase a little in the passive region of the flow since L_θ is growing at a greater rate than L_u (Sirivat & Warhaft 1983), and then decreases

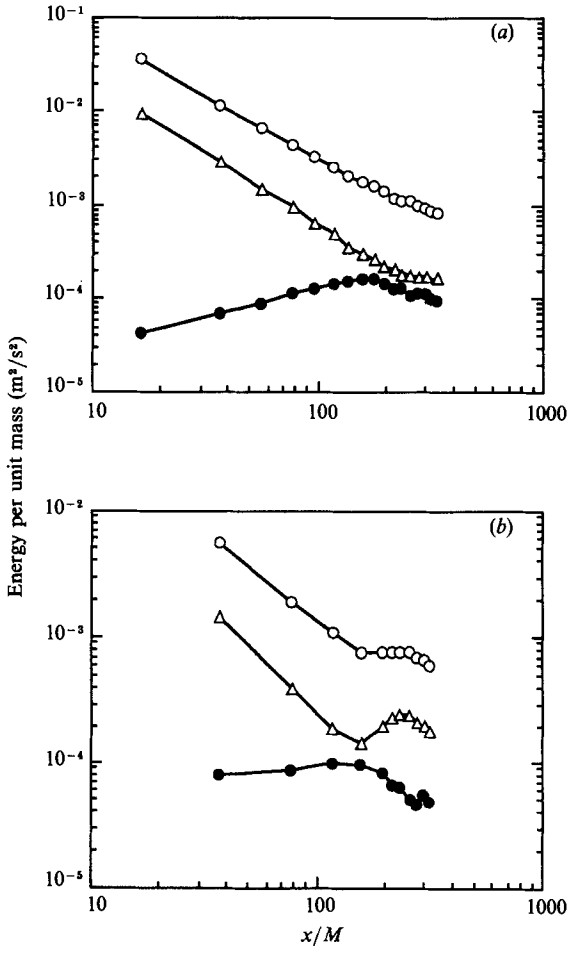

FIGURE 20. The evolution of turbulent kinetic energy, vertical kinetic energy and potential energy. (*a*) $Fr_M = 114$: ○; $\frac{1}{2}(2\overline{u^2}+\overline{w^2})$, △; $\frac{1}{2}\overline{w^2}$, ●; $(g/T_0)(\frac{1}{2}\overline{\theta^2})/\beta$. (*b*) $Fr_M = 84.8$: (symbols are the same as in (*a*)).

as the temperature variance is destroyed by the stable stratification. The peak value is about 0.75 for the data of LV and around 0.6 for our data.

All of the lengthscale ratios shown in figures 18, 19 and 21 show significant quantitative differences between LV and the present experiment. It is this aspect to which we now turn our attention.

As noted earlier, the turbulence time, $\tau = L/(\overline{u^2})^{\frac{1}{2}}$, is proportional to the clock time, $t = x/U$, only when there is a constant exponent (n) velocity power law decay. Close to the grid ($x/M < 40$), and also further downstream, when stratification effects are dynamically important, n varies and t is not proportional to τ. Now as N is increased, the stratification effects become significant at shorter elapsed clock time (or x/M) from the grid. In the present work, for the most stable case ($N = 1.3\ \mathrm{s}^{-1}$; $Fr_M = 84.8$) buoyancy effects do not start to become significant until $x/M \approx 40$, i.e. after the velocity field has settled to a constant power law decay. On the other hand, for the most stable case of LV ($N = 2.42\ \mathrm{s}^{-1}$), buoyancy effects begin to play a role at approximately $10M$ from the grid ($N't \approx 0.1$) and even for their least stable case the distance at which buoyancy effects become important is at less than $30M$. Thus for

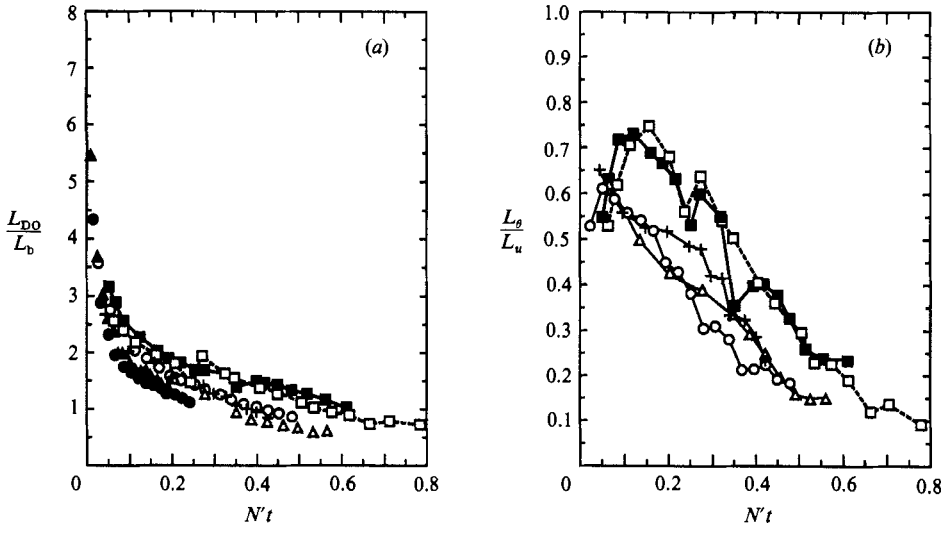

FIGURE 21. The ratio of the Dougherty–Ozimidov lengthscale to the buoyancy lengthscale (L_{DO}/L_b) and the ratio of the over-turning lengthscale to the integral lengthscale (L_θ/L_u). (*a*), L_{DO}/L_b *vs.* $N't$. (*b*) L_θ/L_u *vs.* $N't$. Symbols are the same as in figure 10.

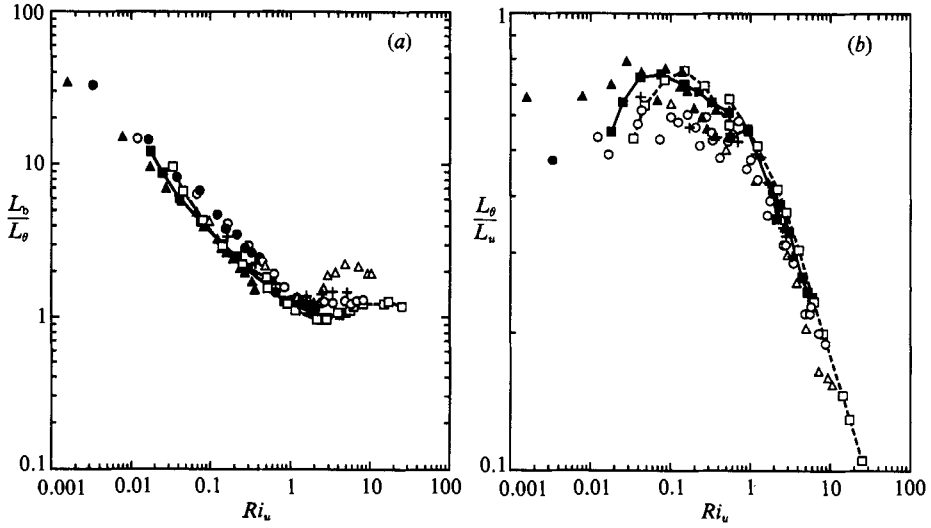

FIGURE 22. L_b/L_θ and L_θ/L_u *vs.* Ri_u. (*a*) L_b/L_θ. (*b*) L_θ/L_u. Symbols are the same as in figure 10.

all of their experiments the buoyancy effects become dominant close to the grid where the wakes of the grid bars are still coalescing and the turbulence decay rate is faster (and hence n is greater) than the power law value observed further downstream. The turbulence time is relatively faster here than the clock time and this explains why the LV data is shifted to the right of our data when plotted as a function of $N't$. These considerations suggest it may be more appropriate to use $N'\tau$ rather than $N't$ to compare the data of the two experiments and this is done in figures 22 and 23 which are plots of L_b/L_θ, L_θ/L_u and Fr_t with $(\tau N)^2 = NL_u/\overline{u^2} = Ri_u$ as the abscissa (note we use $N = 2\pi N'$ for these plots). The collapse is much better than the $N't$ plots

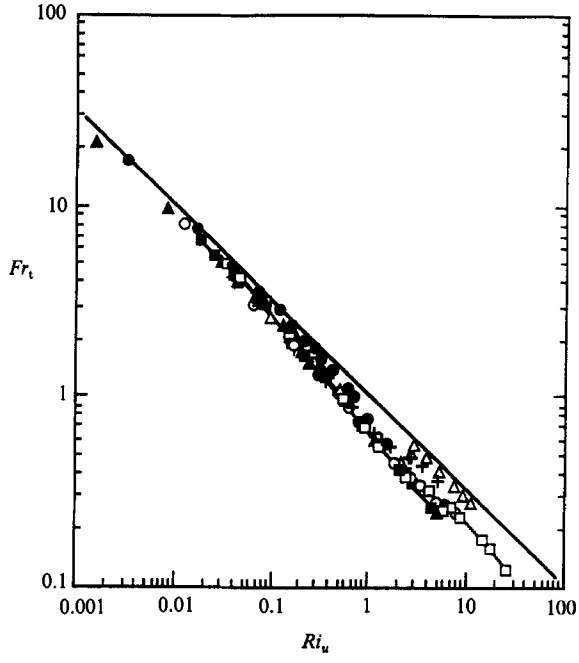

FIGURE 23. Fr_t *vs.* Ri_u. Symbols are the same as in figure 10.

(figures 18, 19 and 21): with the exception of counter heat flux case (for $Ri_u > 2$), the scatter within each data set is now comparable to the differences between the two sets. In terms of the $\rho_{w\theta}$ criteria outlined above for the onset of buoyancy effects ($Fr_t \approx 2; L_b/L_\theta \approx 4$), and for the complete collapse of the heat flux ($Fr_t \approx 0.3$), the transition points in terms of Ri_u are at 0.1 and 2 respectively. Notice that here, as in the previous plots, no premonition of the counter heat flux region for our most stable case is provided by the early evolution of these lengthscale ratios; all cases collapse well up to $Ri_u \approx 2$. Presumably insight into this process could be gained from a study of the dynamics of the spectral transfer between the kinetic and potential energy components at various wavenumbers. This is beyond the scope of the present work. It is clear, however, that as N is increased for our experiments, $\overline{w^2}$ decays more rapidly (figure 4) and the oscillations in the L_b/L_θ and Fr_t curves at large Nt or Ri_u become more pronounced (figures 19, 22*a* and 23).

As noted previously LV do not observe a counter heat flux in their experiments. The reason for this difference is not clear but is presumably due to initial conditions. One possibility is that, as has already been discussed, the buoyancy effects become important very close to the grid in the LV experiment whereas in our work they only become important when the turbulent wakes behind the grid bars have coalesced and the turbulence is close to isotropic. Another possible explanation for this difference between LV and the present work has recently been provided by the direct numerical simulations of Dr M. Rogers (private communication). Rogers shows that if his code is run with substantial initial temperature fluctuations, no counter heat flux occurs downstream, while if the temperature fluctuations develop only as a consequence of turbulent mixing against the temperature gradient (i.e. there are no background temperature fluctuations), a counter heat flux develops at sufficiently high Froude numbers. LV have substantial initial temperature fluctuations (they report values of

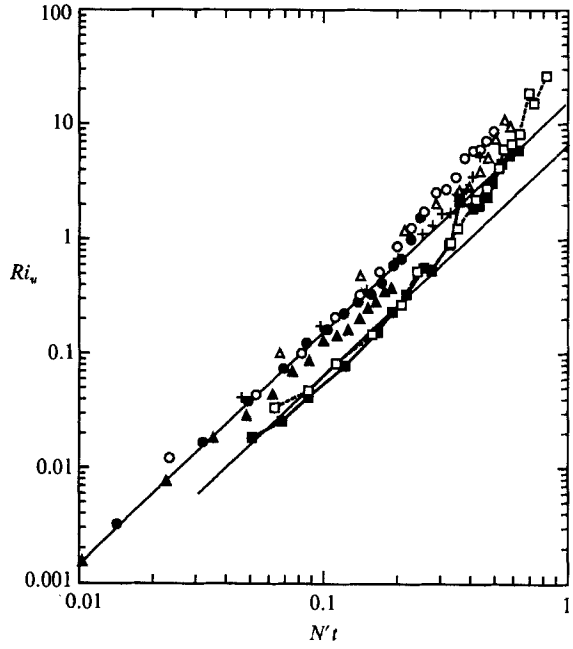

FIGURE 24. Ri_u *vs.* $N't$. Symbols are the same as in figure 10. The straight lines (of slope 2) are the best fit to the present data set and that of LV in the early stages of the flow development ($Ri_u < 0.3$).

± 0.3 °C) compared with less than 0.1 °C in our work. If we use these values to compare the initial fluctuating potential energy to the mean flow energy, $g\overline{\theta^2}/(\beta T_0 U^2)$, the value for LV is approximately five times ours for the most stable case of each experiment. This, then, is another possible indication of the sensitivity of this type of flow to initial conditions.

Note also that $Ri_u = (N^2L^2/\overline{w^2})(\overline{w^2}/\overline{u^2}) = (Fr_t I_{uw})^{-2}$. Thus in figure 23 the departure of the data from a line of slope -0.5 (shown on the graph) indicates the variation of I_{uw} (figure 6) from unity.

The differences between the experiments of LV and our own are further elucidated in figure 24 which is a plot of Ri_u *vs.* $N't$. The best-fit line for the early stages of the flow where buoyancy effects are not too pronounced shows a significant shift between the two data sets: for the same value of $N't$ our experiment exhibits greater dynamic stability in terms of Ri_u, and this is also consistent with the shift in the data of figures 18, 19 and 21.

Another important ratio, for flows with temperature fluctuations, is the mechanical to thermal timescale ratio $r \equiv (2k/\epsilon)/(\overline{\theta^2}/\epsilon_\theta)$. This has been studied extensively for passive scalar turbulence by Warhaft & Lumley (1978) and Sirivat & Warhaft (1983). The latter work shows that, for a passive linear temperature profile its value is around 1.4, indicating that the characteristic timescales for the thermal and velocity fields are approximately the same, at least after the initial thermal field has equilibrated with its own gradient. Figure 25 shows that, for our experiment, the passive value of r of approximately 1.1 is a little lower than for the Sirivat & Warhaft's data. As the flow evolves it remains approximately constant (in LV it declines a little) until the buoyancy effects become very pronounced at $Ri_u \approx 1$ (here $L_b \approx L_\theta$, figure 22*a*). The timescale ratio then begins to increase in the region where

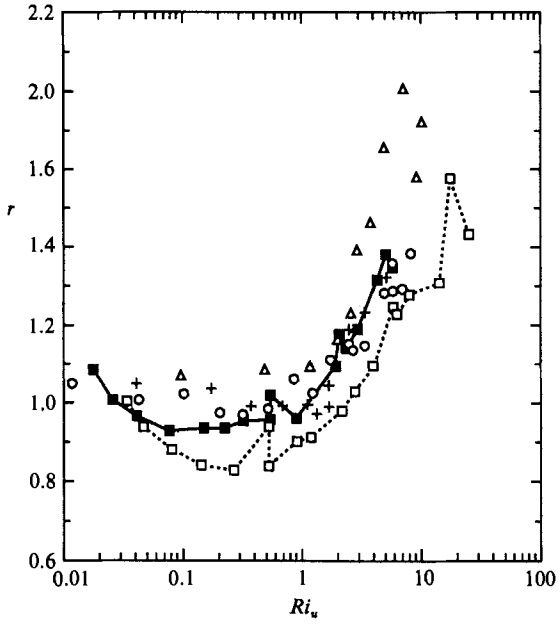

FIGURE 25. The evolution of the mechanical to thermal timescale ratio, r *vs.* Ri_u. Symbols are the same as in figure 10.

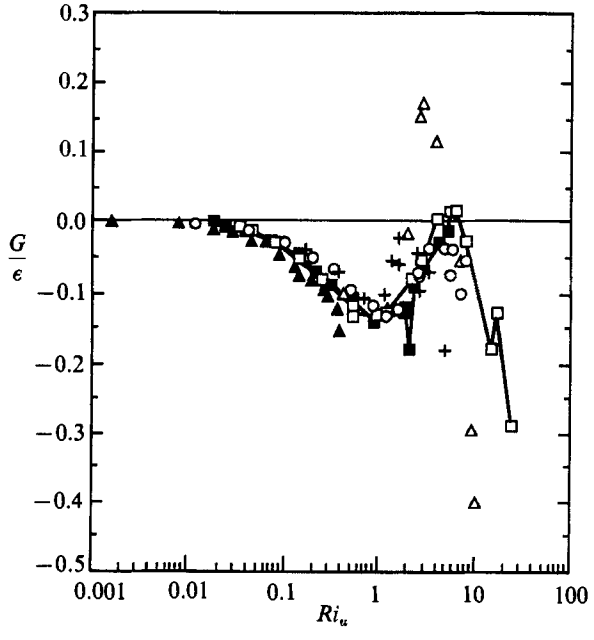

FIGURE 26. The ratio of the buoyancy term ($G = (g/T_0)\overline{w\theta}$) to the dissipation term (ϵ), equation (1), as a function of Ri_u. Symbols are the same as in figure 10.

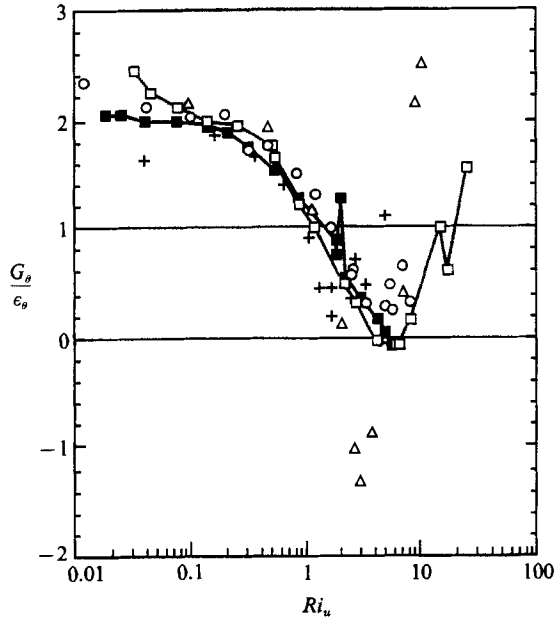

FIGURE 27. The ratio of the flux term ($G_\theta = -\overline{\theta w}\beta$) to the dissipation term (ϵ_θ), equation (3), as a function of Ri_u. Symbols are the same as in figure 10.

the heat flux has collapsed (or whether the counter heat flux occurs). We note that there was a modest increase in the ratio of the thermal lengthscale to the velocity lengthscale in this region also (figure 12*b*). This increase of L_T/L_f is consistent with the increase in r. It is remarkable that r (and L_T/L_f) remain relatively constant up until such a high value of Ri_u (or $N't$).

Our concern until now has been mainly with the interaction of the potential and kinetic energy fields; here we turn our attention to the relative importance of the terms within the rate equations for the turbulent kinetic energy and the fluctuating temperature variance (equations (1) and (3) respectively). Figure 26 shows the ratio of $(g/T_0)\overline{\theta w}, G$, to the mechanical dissipation, ϵ. In stably stratified turbulence G is usually a sink term, but for this flow, it can be a source or sink of kinetic energy, as the figure shows for the most stable case. The ratio initially declines (from its passive value of zero) as the mechanical dissipation becomes less intense and the gravitational term assumes a more dominant role. The minimum of approximately -0.13 is reached at $Ri_u \approx 1$ and the ratio then increases and approaches zero as the heat flux completely collapses at $Ri_u \approx 2$ (figure 28). For higher values of Ri_u there is scatter in the data but, for most cases, the ratio decreases as the gravitational flux term begins to act as a sink of kinetic energy again. For the most stable case, however, G/ϵ becomes positive in the counter heat flux region. Its large value of nearly 0.2 shows that for a brief period the relative strength of the heat flux term as a source is greater than its strength as a destruction term in any other (upstream) region of the flow.

Similar trends are shown in figure 27, which is the ratio of the flux gradient term $(-\overline{\theta w}\beta)$ to the thermal dissipation rate $(\epsilon_\theta), G_\theta/\epsilon_\theta$, (equation (3)). Note that when $G_\theta/\epsilon_\theta = 1$, the rate of destruction of temperature variance starts to exceed its production rate and the advection term (left-hand side of equation (3)) changes sign.

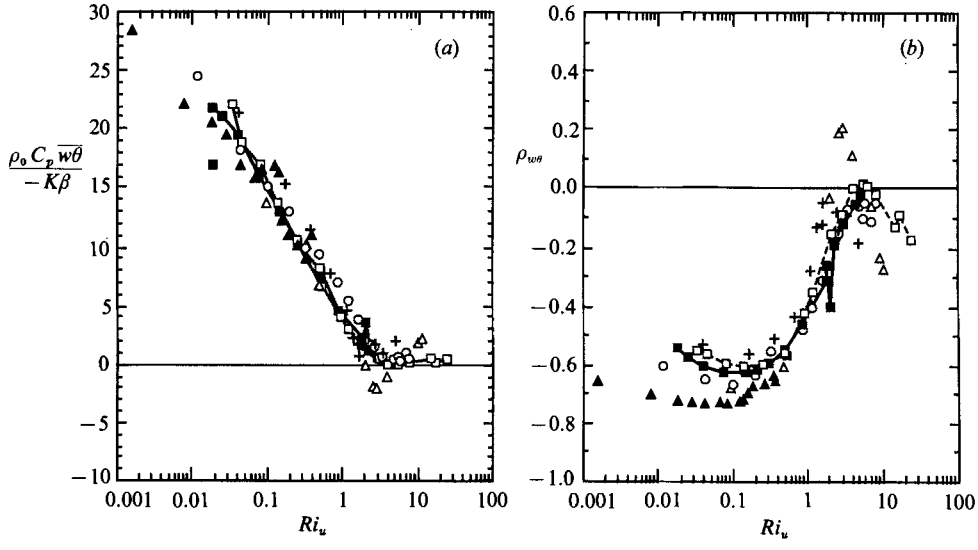

FIGURE 28. The ratio of the turbulent heat flux to molecular heat flux (*a*) and the heat flux cross correlation coefficient, $\rho_{w\theta}$, (*b*) plotted as a function of Ri_u. Symbols are the same as figure 10.

This occurs at $Ri_u \approx 1$. Both in this and the previous figure there is good collapse of our data with that of LV (with the exception of our counter-gradient heat flux case).

Finally, figure 28 shows the ratio of turbulent heat flux to molecular heat flux, and the heat flux correlation coefficient, $\rho_{w\theta}$, plotted as a function of Ri_u. The agreement with LV is better than when the data is plotted as a function of $N't$ (figure 14), with the exceptions (noted above) of the counter heat flux case and the higher initial $\rho_{w\theta}$ in the present work.

6. Conclusions

The effects of stable stratification on the evolution of grid-generated turbulence are profound, producing a complex interaction between the fluctuating kinetic energy and potential energy fields that can completely suppress turbulent transport and even result in regions of counter gradient heat flux. In this study, using a new large low-speed wind tunnel, the mesh Froude number $Fr_M = U/(NM)$ was varied (by means of changing both the mean speed and temperature gradient) from ∞ (passive temperature gradient) to 84.8 ($\mathrm{d}T/\mathrm{d}z = 55$ °C/m). In terms of turbulence quantities, $Ri_u\,(=N^2L^2/\overline{u^2})$ extended to 10 at the furthest downstream station for the most stable case. The data were found to scale best with Ri_u (the square of the ratio of the turbulent to stratification time), but, for comparison with previous work we have also stated our results in terms of non-dimensional clock time, $N't$. First we will summarize our results and we will then compare them with previous work.

Our main findings are as follows. Up until $Ri_u \approx 0.1$ ($N't \approx 0.08$) the flow is close to being dynamically passive; the heat flux cross-correlation coefficient $\rho_{w\theta}$ remains constant at approximately -0.7 (figure 14*b*) and turbulence field decays in the same way as for neutral turbulence. Our results for this early region of the flow development compare well with the passive linear gradient experiments of Sirivat & Warhaft (1983). At $Ri_u \approx 0.1$ the fluctuating potential energy has increased to

approximately 5% of the vertical kinetic energy ($L_b/L_\theta \approx 4$, figure 22*a*, $Fr_t \approx 3$, figure 23) and from there on its increasing importance results in the decay of the heat flux (figure 14) and a more rapid decay of the vertical velocity variance (figure 4). The ratio of the buoyancy to dissipation terms in the kinetic energy budget (figure 26) also gradually decreases from its initial value of zero and reaches its minimum at $Ri_u \approx 1$; it then rapidly returns to zero.

By $Ri_u \approx 2$ ($N't \approx 0.3$) the heat flux has completely collapsed. Thereafter it either reverses sign and becomes counter gradient or it gradually increases again (figures 14 and 28). The counter gradient heat flux only occurred for the strongest stratification investigated ($Fr_m = 84.8$). For this case the data still scales well with the other data up to $Ri_u \approx 2$ (figures 22–28) but for higher Ri_u (or $N't$) the correlation coefficient and flux change sign (figure 14) and thus there are significant differences compared to the less strongly stratified experiments. We do not know what parameter determines when the heat flux will become counter gradient, apart from the fact that it occurs only for our most stable experiment and that it is associated with the rapid decay of $\overline{w^2}$ earlier in the flow development (figure 4). For this (counter-heat flux) case the vertical velocity variance increases in the region where the counter gradient heat flux occurs and the gravitational term (in the kinetic energy equation) reverses sign and becomes a source of kinetic energy while the corresponding term in the potential energy budget becomes a sink. For all the stably stratified cases, for $Ri_u > 2$ ($N't > 0.3$), the temperature fluctuation dissipation rate (figure 13) decays rapidly, with a power law decay exponent of approximately -2 compared with -0.33 in the region $Ri_u < 1$, as the temperature variance is destroyed by the buoyancy (figure 10). There is a significant, but less dramatic increase in the rate of dissipation of turbulent kinetic energy in this region (figure 9).

The ratio of the longitudinal to vertical r.m.s. velocity fluctuations, I_{uw} increases from its neutral valve (of 1.1) as the buoyancy effects become pronounced, reaching a maximum at approximately $Ri_u \approx 1$ ($N't \approx 0.3$, figure 6) where the production to dissipation has peaked (figure 26), thereafter decreasing as the heat flux collapses. The results suggest that I_{uw} is not an indicator of anisotropy in a flow such as this. The lengthscale ratios formed from the longitudinal and vertical autocorrelation functions and spectra showed much scatter but there is some evidence that as the heat flux collapses the vertical velocity fluctuations increase in size relative to the longitudinal fluctuations (figure 8).

Particular attention has been paid to comparing the present work with the results of Lienhard & Van Atta (1990), the only other strongly stratified wind-tunnel experiment that we are aware of. We show that when the two data sets are plotted as a function of $N't$ one data set is shifted with respect to the other (e.g. figures 18 and 19). However, if the turbulence time is used rather than the clock time, i.e. the data are plotted as a function of Ri_u ($= (N\tau)^2$) the collapse of the data is much better (e.g. figures 22 and 23). We attribute the difference between the data sets largely to the higher values of N used by LV which causes the buoyancy effects to become significant very close to the grid while the turbulence is still forming and the constant power law decay has not yet been attained. Another significant difference between the two experiments is that LV do not observe a region of net counter gradient heat flux; in their experiment $|\rho_{w\theta}|$ tends to fall to zero and then begins to increase again (figure 14). Thus they do not find a region where $\overline{w^2}$ increases with downstream distance, as we do. The reason for these differences is less certain but again may be due to initial conditions. We note that the direct numerical simulations of Riley *et al.* (1981) do show a region of counter gradient heat flux, and oscillations in $\overline{w^2}$, and

these occur at approximately the same non-dimensional time as in our experiments. Riley *et al.* also find, as do we, that the fluctuating potential energy never reaches the level of the vertical kinetic energy while LV find these become equal ($L_b = L_\theta$) as $N't$ increases. On the other hand, the stratified salt-water experiments of Stillinger *et al.* (1983) and Itsweire *et al.* (1986) show L_θ becomes larger than L_b, as do the numerical simulations of Métais (1987). The salt-water experiments also exhibit regions of counter gradient heat flux in common with our experiments. We note however, as do LV, that there are many differences between the air and salt water experiments, apart from the vastly different Prandtl numbers. In particular the salt stratified experiments exhibit strong gravity wave effects while for the air experiments, of both LV and the present work, direct evidence of them is lacking. Presumably more subtle detection methods (such as multipoint measurements) will be needed to reveal them.

We wish to thank Mr E. P. Jordan for his enthusiastic technical assistance in constructing the wind tunnel. We also thank Professors Van Atta and Lienhard for preprints of their work and the referees for helpful comments. This work was supported by grants from the Department of Energy (Basic Energy Sciences, DE-FG02-88ER13929) and the US National Science Foundation (Atmospheric Science, ATM-8412558).

REFERENCES

AXFORD, D. N. 1971 Spectral analysis of an aircraft observation of gravity waves. *Q. J. R. Met. Soc.* **97**, 313–321.

BENDAT, J. S. & PIERSOL, A. G. 1971 *Random Data: Analysis and Measurement Procedures.* Wiley.

BRITTER, R. E., HUNT, J. C. R., MARSH, G. L. & SNYDER, W. H. 1983 The effect of stable stratification on turbulent diffusion and the decay of grid turbulence. *J. Fluid Mech.* **127**, 27–44.

BUDWIG, R., TAVOULARIS, S. & CORRSIN, S. 1985 Temperature fluctuations and heat flux in grid-generated isotropic turbulence with streamwise and transverse mean temperature gradients. *J. Fluid Mech.* **153**, 441–460.

CAUGHEY, S. J. 1977 Boundary layer turbulence in stable conditions. *Boundary Layer Met.* **11**, 3–14.

CHAMPAGNE, F. H. & SLEICHER, C. A. 1967 Turbulence measurements with inclined hot-wires. Part 2. hot-wire response equations. *J. Fluid Mech.* **28**, 177–182.

CHAMPAGNE, F. H., SLEICHER, C. A. & WEHERMANN, O. H. 1967 Turbulence measurements with inclined Hot-wires. Part 1. Heat transfer experiments with inclined hot-wires. *J. Fluid Mech.* **28**, 153–176.

COMTE-BELLOT, G. & CORRSIN, S. 1966 The use of contraction to improve the isotropy of grid-generated turbulence. *J. Fluid Mech.* **25**, 657–682.

COMTE-BELLOT, G. & CORRSIN, S. 1971 Simple Eulerian time correlation of full and narrow-band velocity signals in grid-generated, 'isotropic' turbulence. *J. Fluid Mech.* **48**, 273–337.

CORRSIN, S. 1952 Heat transfer in isotropic turbulence. *J. Appl. Phys.* **23**, 113–118.

DICKEY, T. D. & MELLOR, G. L. 1980 Decaying turbulence in neutral and stratified fluids. *J. Fluid Mech.* **99**, 13–31.

DOUGHERTY, J. P. 1961 The anisotropy of turbulence at the meteor level. *J. Atmos. Terr. Phys.* **21**, 210–213.

ELLISON, T. H. 1957 Turbulent transport of heat and momentum from an infinite rough plane. *J. Fluid Mech.* **2**, 456–466.

GIBSON, C. H. 1980 Fossil temperature, salinity and vorticity in the ocean. In *Marine Turbulence* (ed. J. C. T. Nihoul), p. 221. Elsevier.

GIBSON, C. H. 1987 Fossil turbulence and intermittency in sampling oceanic mixing processes. *J. Geophys. Res.* **92**, no. C5, 5383–5404.

HINZE, J. O. 1975 *Turbulence*, 2nd edn. McGraw-Hill.

HOPFINGER, E. J. 1987 Turbulence in stratified fluids: A review. *J. Geophys. Res.* **92**, no. C5, 5287–5303.

HUNT, J. C. R. 1985 Diffusion in the stably stratified atmospheric boundary layer. *J. Climate Appl. Met.* **24**, 1187–1195.

HUNT, J. C. R., KAIMAL, J. C. & GAYNOR, J. E. 1985 Some observations of turbulence structure in stable layers. *Q. J. R. Met. Soc.* **111**, 793–815.

ITSWEIRE, E. C., HELLAND, K. N. & VAN ATTA, C. W. 1986 The evolution of grid-generated turbulence in a stably stratified fluid. *J. Fluid Mech.* **162**, 299–388.

KOLMOGOROV, A. N. 1941 Energy dissipation in locally isotropic turbulence. *Dokl. Akad. Nauk SSSR* **32**, no. 1, 19–21.

LIENHARD, J. H. 1988 The decay of turbulence in thermally stratified flow. PhD dissertation, University of California at San Diego.

LIENHARD, J. H. & VAN ATTA, C. W. 1990 The decay of turbulence in thermally stratified flow. *J. Fluid Mech.* **210**, 57–112.

LUMLEY, J. L. & PANOFSKY, H. A. 1964 *The Structure of Atmospheric Turbulence*. Interscience.

MÉTAIS, O. 1987 Turbulence submitted to stable density stratification: large eddy simulation and statistical theory. *Sixth Symposium Turbulent Shear Flows, Sept. 7–9, Toulouse.*

MONIN, A. S. & YAGLOM, A. M. 1971 *Statistical Fluid Mechanics*, vol. 1. MIT Press.

MONTGOMERY, R. D. 1974 An experimental study of grid turbulence in a thermally-stratified flow. PhD dissertation, University of Michigan.

OZMIDOV, R. V. 1965 On the turbulent exchange in a stably stratified ocean. *Izv. Atmos. Oceanic Phys.* ser. 1, **8**, 835–860.

PEARSON, H. J., PUTTOCK, J. S. & HUNT, J. C. R. 1983 A statistical model of fluid element motions and vertical diffusion in a homogeneous stratified fluid. *J. Fluid Mech.* **129**, 219–249.

PERRY, A. E. 1982 *Hot Wire Anemometry*. Oxford University Press.

RILEY, J. J., METCALFE, R. W. & WEISSMANN, M. A. 1981 Direct numerical simulation of homogeneous turbulence in density-stratified fluids. In *Nonlinear Properties of Internal Waves* (ed. B. J. West). *AIP Conf. Proc.* vol. 76, pp. 79–112.

SANDERSON, R. C., HILL, J. C. & HERRING, J. R. 1987 Transient behavior of a stably stratified homogeneous fluid. In *Advances in Turbulence* (ed. G. Comte-Bellot & J. Mathieu). Springer.

SIRIVAT, A. & WARHAFT, Z. 1983 The effect of a passive cross-stream temperature gradient on the evolution of temperature variance and heat flux in grid turbulence. *J. Fluid Mech.* **128**, 323–346.

STEWART, R. W. 1969 Turbulence and waves in a stratified atmosphere. *Radio Sci.* **4**, 1269–1278.

STILLINGER, D. C., HELLAND, M. J. & VAN ATTA, C. W. 1983*b* Experiments on the transition of homogeneous turbulence to internal waves in a stratified fluid. *J. Fluid Mech.* **131**, 91–122.

STILLINGER, D. C., MEAD, M. J., HELLAND, K. N. & VAN ATTA, C. W. 1983*a* A closed-loop gravity-driven water channel for density stratified shear flows. *J. Fluid Mech.* **131**, 73–89.

TENNEKES, H. & LUMLEY, J. L. 1972 *A first course in turbulence*. MIT Press.

TURNER, J. S. 1973 *Buoyancy Effects in Fluids*. Cambridge University Press.

VENKATARAMANI, K. S. & CHEVRAY, R. 1978 Statistical features of heat transfer in grid-generated turbulence: constant gradient case. *J. Fluid Mech.* **86**, 513–543.

WARHAFT, Z. & LUMLEY, J. L. 1978 An experimental study of the decay of temperature fluctuations in grid-generated turbulence. *J. Fluid Mech.* **88**, 659–684.

WEBSTER, C. A. G. 1964 An experimental study of turbulence in a density stratified shear flow. *J. Fluid Mech.* **19**, 221–245.

WEIGHART, K. E. G. 1953 On the resistance of screens. *Aero. Q.* **4**, 186.

YOON, K. 1989 The effect of stable stratification on decaying grid-generated turbulence. PhD dissertation, Cornell University.